TRANSPORT OF RED AND WHITE BLOOD CELLS IN WHOLE BLOOD MICROFLOWS FOR MICROFLUIDICS-BASED, IN-VITRO DIAGNOSTICS APPLICATIONS

A DISSERTATION
SUBMITTED TO THE FACULTY OF
UNIVERSITY OF MINNESOTA
BY

DANIEL R. MCPEAK

IN PARTIAL FULFILLMENT OF THE REQUIREMENTS
FOR THE DEGREE OF
DOCTOR OF PHILOSOPHY

DR. EPHRAIM SPARROW, ADVISER

December, 2015

Acknowledgements

I would like to thank my advisor for pushing me to work beyond my personal strengths and for his valued wisdom in scientific and personal endeavors. Thanks for everything, Eph.

I would like to thank all of the employees of Ativa Medical; the opportunity to work with you all is a true blessing.

Special thanks go to Eric Peltola, Taha Najmee, and Karman Lee who have been incredible friends and collaborators throughout this project.

Finally, love and thanks to my wonderful family.

Dedication

This thesis is dedicated to my family.

Abstract

The research set forth in this thesis was motivated by the desire to create a microfluidic device for measuring cell concentrations in whole blood. Such a technology would enable the creation of important point-of-care diagnostic tests such as the Complete Blood Count. The path of investigation documented in this thesis was not carried out in a predetermined manner. But rather, the collected thoughts and experiments were spurred on by obstacles encountered in the pursuit of the desired technology. **While the realization of a cell-enumerating device is of key interest, it was found—and is shown—that much of the challenge in creating such a device lies in addressing innate properties of the blood sample itself**. As a consequence, investigation of these properties and their importance with regard to micro-scale cell transport is the primary technical focus of the research. Herein, it is shown that cell transport in creeping whole blood micro-flows is dominated by interphase flow brought about by phase-density imbalances and the elevated Darcy permeability which is associated with erythrocyte aggregation in low-shear flows. Additionally, non-uniform distribution of cells and the non-Newtonian properties of whole blood are hypothesized to affect the transport of white blood cells in situations where the rate of bulk flow changes appreciably. Study of these effects by way of experimentation and the development of mathematical descriptions of cell transport ultimately led to the creation of a device which circumvents deleterious consequences of whole blood behavior and achieves accurate quantitation of red and white blood cell concentrations.

Table of Contents

List of Tables

List of Figures

Chapter 1: Introduction

The present research is concerned with the characterization of whole blood dynamics which are pertinent to microfluidic devices such as those found within point-of-care (POC) *in-vitro* diagnostics applications. Specifically, emphasis is placed upon experimental analysis of cell transport in sub-millimeter-scale blood flows. There are two benefits to be derived from this research: first, said analyses expand the fundamental understanding of whole blood behavior; this is especially relevant from the viewpoint of microfluidic point-of-care devices. Secondly, the experimental results inform the refinement of the particular microfluidic technology which had inspired this research: a microdevice for quantifying cell concentrations in whole blood. Because this technology enables the development of POC cell-counting assays such as a Complete Blood Count, the technical advancements of this research should enhance the scope of diagnostic tests available for use at the point-of-care and in turn contribute to the efficacy and accessibility of medical diagnostic services, worldwide.

1.1 Motivation

The motivation behind this research is rooted in the global need for improved access to high-quality, medical diagnostic services. Though diagnostic testing accounts for a relatively small financial fraction of modern healthcare systems, diagnostics influence

between (60-70%) of clinical decisions [1]. According to the World Health Organization (WHO), accessibility to diagnostic testing is especially lacking in developing countries with high disease burdens. Additionally, The WHO states that three of the primary reasons for poor accessibility in low-access regions include: excessive financial burden to patients, lack of trained personnel to operate equipment, and long distances separating patients from the nearest laboratory [2]. Presently, the medical community is addressing these issues with the development of point-of-care diagnostic technologies which are economical, easy-to-use, and distributable such that the technologies can be utilized in small, dispersed locations like general practitioners' offices and health clinics [3]. As a result of this distribution of medical diagnostic services, informed diagnosis should be provided to more patients and with greater efficiency than is possible within existing healthcare systems [4].

In established healthcare systems within which diagnostics accessibility is not of significant concern, point-of-care testing is targeted more for its impact on workflow efficiency. For example, a 2004 study comparing point-of-care and central-laboratory glucose measurements (both methods being performed within a single hospital) demonstrated that the financial and labor burdens were approximately halved through the of POC testing [5]. In this case, much of the benefit of the POC test related to steps which were eliminated from the workflow: sample transport, laboratory receiving, and manual result reporting.

Workflow efficiency is also the driving force behind the adoption of POC testing by general practitioners and health clinics. However, the desired efficiency in these settings pertains more to the minimization of the time between first patient contact and an informed diagnosis. With tests available at the point-of-care, practitioners can utilize established diagnostic procedures as part of their normal office-visit workflow. Subsequently, patients receive informed diagnosis and are prescribed treatment with a single visit to their provider. These benefits are forfeit when a patient's condition requires testing which is unavailable at the point of care. Under such circumstances, the provider must rely on the traditional sources of diagnostic testing wherein the patient is referred to a hospital laboratory or a specimen is acquired and sent to a centralized testing facility. In either of these scenarios, diagnosis and treatment are delayed and both the patient and provider are burdened with follow-up from their initial contact.

One manner of advancement of the point-of-care movement, then, can be thought of as reduction of the likelihood that healthcare providers find themselves without the desired testing equipment. Toward that end, the aim of the technology explored within this research is to provide POC practitioners with tests requiring quantification of blood cell concentrations, such as the Complete Blood Count. Presently, there is a need for a Complete Blood Count technology which satisfies the economics and ease-of-use necessitated by the point-of-care model. The Complete Blood Count (CBC), which provides an overview of a patient's blood composition, serves a key role in the medical

diagnostic process as supported by Medicare's list of the 100 most-frequently-utilized procedures for 2007 [6] wherein the CBC is shown to be the most common blood test utilized within the Medicare system. Without the CBC available at the point-of-care, there is a critical element missing from the de-centralization of medical diagnostics. As such, research contributing to the development of point-of-care CBC technologies might advance POC testing as a whole.

1.2 Point-of-Care Diagnostics Technology

Point-of-care testing (POCT) is a rapidly-developing area of medical technology which aims to equip general practitioners and health clinics with health analytics that were traditionally only readily-accessible to hospital staff [7]. In 2010, the National Institute of Health released a memo regarding the past, present and future status of the point-of-care movement. In this report, the NIH stated that "Empowering clinicians to make decisions at the "point-of-care" has the potential to significantly impact health care delivery and to address the challenges of health disparities" [8]. With respect to the progression of point-of-care testing, the NIH recognizes "the development of miniaturized devices" as a critical endeavor. 'Devices' here refers to any in a spectrum of technologies, each of which has a set of characteristics which define its role in the diagnostic process. In Figure 1-1, POC technologies are segmented into six categories ranging from retail-grade dipstick tests (labeled 'Disposable') to sophisticated wearable and benchtop instruments.

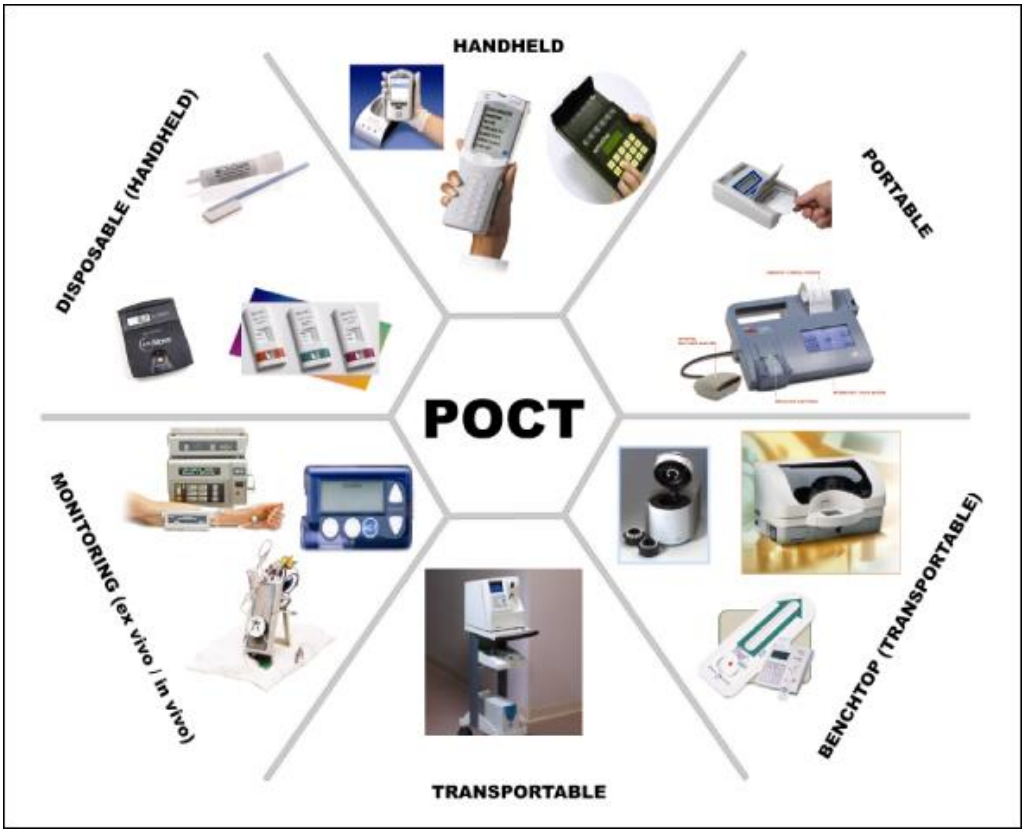

Figure 1-1. From [9]: Diagram of POCT technology categories

From the viewpoint of a retail consumer, the disposable category of diagnostic devices is most familiar; a segment which includes pregnancy tests and glucose strips, the latter of which allows diabetics to monitor and subsequently control their blood sugar level. As a general rule, affirmed by loose standards set forth by regulating entities, the 'disposable' technologies are measurably less accurate than laboratory-grade equivalents. For instance, glucose strips are only required by the International Standards Organization (ISO) to provide readings that are within ±15% of a laboratory reference value [10]. This standard is substantially less stringent than claimed accuracy of a common handheld instrument, the Abbott iStat, which produces glucose measurements which are within

±5% of reference values [11]. Still, the standard established for glucose strips ensures that they are sufficiently accurate to serve their claimed purpose: to inform a diabetic if their blood glucose level is low--requiring sugar intake, high--necessitating a dose of insulin.

A device's ability to support its claimed purpose is the primary concern of the POC practitioner and is a key differentiator between POC tests within the disposable category and those without. The intended use of laboratory-grade POC technologies, to guide diagnosis and treatment, necessitates a high level of accuracy. The challenge of POC technologies, then, is to bridge the performance gap between lab-grade and disposable technologies such that the ease-of-use of disposable technologies can be achieved without sacrificing diagnostic integrity. In this research, focus is placed on one form of lab-grade POC technology--microfluidic devices--which performs sample processing in low-cost, one-time-use fluidic circuits which should enable the ease-of-use of Disposable technologies while achieving measurement accuracy equivalent to clinical laboratory instruments.

1.3 Microfluidics

Microfluidics refers to technologies which utilize precisely-controlled, micro-scale fluid flows. Microfluidic circuits are leveraged in a variety of applications such as fuel cells, inkjet printers, and labs-on-a-chip. Lab-on-a-chip (LOC) technologies are intended to perform clinical laboratory procedures in an automated fashion through the utilization of

micro-scale fluidic circuits which replace the inner workings of larger, traditional lab equipment.

In 2011, a critical review of point-of-care diagnostic research recognized that "A variety of theoretical models and academic proof-of-concept studies have demonstrated tantalizing advantages of lab-on-a-chip systems…" [12]. However, the authors go on to note "surprisingly few LOC-based diagnostic tests have been successfully introduced into the market." Furthermore, this publication specifies the key challenges which include "new methods for sample collection, world-to-chip interfaces, sample pre-treatment, improvement of long-term stability of reagents and working with complex sample specimens (such as whole blood, stool, swabs, sputum, tears, and saliva)." The present research shall address one facet of the problem of manipulating "complex samples" by characterizing the physics of cell transport in whole blood micro flows.

1.4 Research Overview

This research consists of a series of experiments aimed at the characterization of red and white blood cell transport in whole blood flows which are contained within a LOC microdevice. In each experiment, the bulk volumetric flow rate of blood is controlled by an off-device pumping system. Control of the bulk volumetric flow rate allows comparison of experimentally-measured transport rates with the desired descriptor of cell transport within the flow, given in Equation (1-1). Equation (1-1) states that the rate at which a given cell type is transported within a whole blood flow should be described as

the product of the bulk whole blood flow rate and the concentration of the cell type within the blood sample. A derived form of Equation (1-1) is often used to describe advective transport in gaseous and liquid mixtures. However, given that whole blood is a colloidal suspension, this description is not necessarily applicable and it is important that the transport system satisfy the principal assumption of the equation: that the ratio of volumetric transport for each phase is equal to its whole-blood volume fraction. The primary technical aim of this research is to identify whole blood phenomena which violate this assumption and to invent the means for negating the deleterious effects of said phenomena.

$$\dot{n}_{transported} = c_i * \dot{V}_{Whole\ Blood} \quad (1\text{-}1)$$

The experimental apparatus which enables this investigation is described in Chapter 2. To support the accuracy of gathered data, this chapter provides detail regarding calibration of the sensor which controls the volumetric flow rate of whole blood. Furthermore, Chapter 2 contains an overview of microdevice components and an explanation of the process by which the fluidic circuit enables quantification of blood cell concentration. It should be noted that the device depicted in Chapter 2 is one of multiple unique designs utilized within this research. Individual devices are detailed at the beginning of the appropriate chapter; the overview in Chapter 2 provides an explanation of the measurement methodology and understanding of how the circuit components function.

In Chapter 3, an initial microdevice design is introduced. The overview of this device focuses on the device's fluidic features while simultaneously providing an explanation of the sample analysis procedure. Additionally, Chapter 3 details the experimental testing of this initial device design and provides some general comments regarding the results from this testing.

The data generated in Chapter 3 is analyzed in Chapter 4. Telling trends in the data are compared with established Hemorheological research as a means to generate working hypotheses for subsequent investigation. Specifically, erythrocyte sedimentation is shown to be a likely cause of non-linearity observed in both RBC and WBC concentration measurements produced by the initial microdevice design.

The working hypotheses generated in Chapter 4 are expanded upon in Chapter 5 where two secondary modes of transport are detailed. The first phenomenon described is primarily applicable to white blood cell transport: Inhomogeneous distributions of white blood cells within the red blood cell matrix and the non-Newtonian properties of whole blood are expected to produce a piecewise shift in white blood cell transport due to the potential for a shift in average WBC channel-wise velocity which is disproportionate to the shift in bulk volumetric flow rate that occurs between the device-loading and cell-dispensing processes. The second phenomenon is an overriding consideration with regard to the sedimentation process: Shear has been shown to affect the sedimentation

rate with sedimentation rates equal to the ESR value under low-shear conditions, elevated sedimentation over a middle shear range, and a diminishing sedimentation rate above a peak-sedimentation shear rate. While the data from Chapter 3 are strongly indicative of sedimentation effects, little indication of these secondary effects is afforded by experimental data and the phenomena presented in Chapter 4 are treated as cautionary considerations for the subsequent microdevice optimization.

In Chapter 6, a gravity-negating transport domain is devised as a means to achieve accurate quantitation of red and white blood cell concentration via the cell-dispensing process. The basic premise of the optimized cell-dispensing technology leverages the 'suspension' region of a sedimenting body as a source from which untainted specimen can be siphoned. It is shown that the relatively-stable spatial distribution of cells in that region and a gravity-perpendicular outlet velocity can produce an outlet transport rate that agrees with Equation (1-1). After detailing the physical premise of the gravity-negating transport domain, an optimized microdevice, making use of this transport domain, is described. As a conclusion to Chapter 6, the optimized microdevice is tested using a comparability-study format in order to gauge the efficacy of the gravity-negating transport domain. Ultimately, the data generated by this device suggest a flaw in the operation of the revised transport domain.

Chapter 7 expands the understanding of whole blood dynamics within the cell-transport domain to include considerations for channel elements beyond the sedimenting domain. In particular, numerical simulation is used to demonstrate that the geometry of post-outlet passages can produce plasma recirculation which compromises the domain working principles. In turn, a revised post-outlet configuration is simulated and shown to produce a stably, forward-moving outlet flow. Subsequently, a new microdevice design is created which incorporates the revised post-outlet geometry. Testing of this device yields RBC and WBC concentration measurements which are substantially more accurate than measurements generated by each of the previously-tested designs.

Chapter 2: Technical Overview of Experimental Apparatus and Microdevice Composition

2.1 Experimental Apparatus

The microdevices studied within this research are 'passive' meaning that the physical devices contain no internal mechanisms for propelling fluids or for performing cell detection. To compensate for the lack of these functionalities, devices are coupled with an external pumping system which drives in-device flows and an optical-detection system which facilitates the quantitation of cell transport rates. Interaction of the device with the pumping and optical detection systems are shown schematically in Figure 2-1. As illustrated be this figure, a device facilitates three sequential operations—cell dispensing, cell processing, and cell focusing—and that each of these operations is complemented by the delivery of a fluid stream by the pumping system.

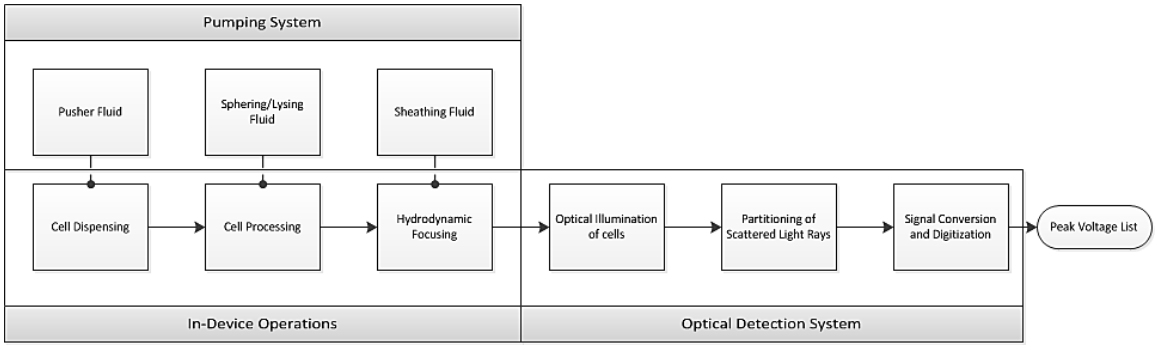

Figure 2-1. Schematic overview of device interaction with pumping and optical-detection systems

The first fluid is a ‘pusher’ fluid which flows into the cell-dispensing portion of the microdevice and displaces the whole blood which is pre-loaded into that volume. The second fluid is a processing reagent; ‘sphering’ solution which bloats red blood cells (spherical cells are more conducive to analysis) or ‘lysis’ solution which destroys red blood cells such that white blood cells are more readily detected. The final fluid is a ‘sheathing’ solution which is used to hydrodynamically focus (read: align cells in the channel-spanwise direction) cells at the point of detection.

As focused cells pass through the point of detection, the optical detection system illuminates individual cells with a laser beam. The transit of cells through the beam results in light scattering. Select portions of the scattered light are focused onto photodiodes which produce an electric current proportionate to the intensity of received light. This current is converted to a proportionate voltage using a trans-impedance amplifier. As a cell passes through the laser beam, the intensity of scattered light rises, reaches a peak value corresponding to the peak beam intensity, and then falls as the cell exits the beam. The resulting voltage pulse undergoes a peak-finding operation. Ultimately, the optical detection system produces a list of the peak voltage values for cells which transit the beam during a ‘measurement’ operation.

2.1.1 Fluid Pumping System

The present research plan and the technology it aims to refine both rely upon knowledge of volumetric rates of in-device flows. To satisfy those needs, the experimental apparatus

includes a pumping system which consists of four piston pumps which are individually actuated by stepper motors—Sapphire Engineering's V-series pump. Each of the four pumps dispenses fluid through a Sensirion LG16-series flow sensor which provides a digital reading of the volumetric flow rate with a characteristic response time of (40 [ms]) [13]. The flow readings serve as the output variable for a PID-controller which determines the rate of piston displacement based on the difference between sensor readings and the volumetric flow rates specified by an automated routine. A diagram of a pump-controller loop is provided in Figure 2-2 which shows the flow of fluid from a piston pump, through a flow sensor, and an outlet flow which is ultimately supplied to a microdevice.

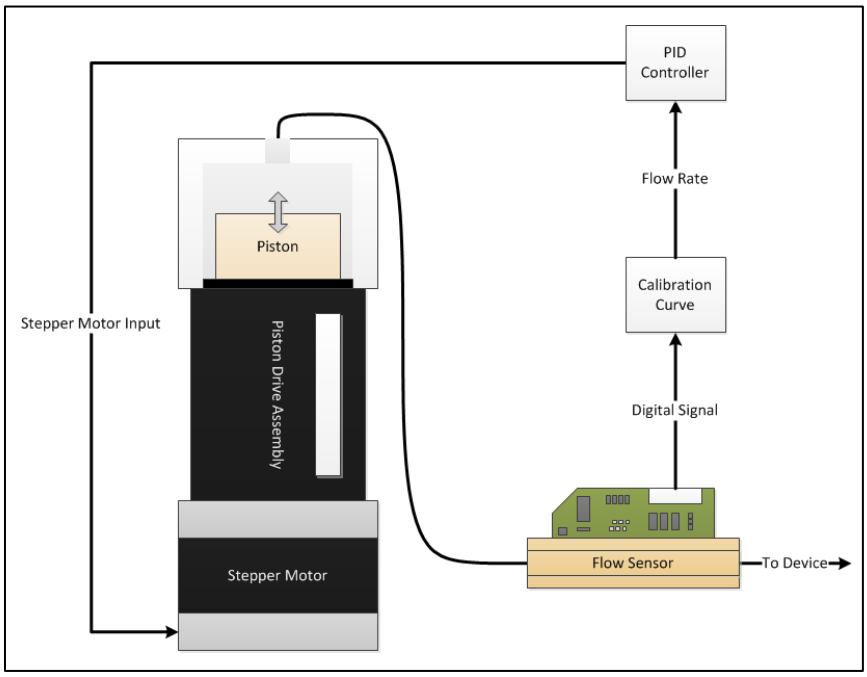

Figure 2-2. Diagram of PID-controlled pump

Also indicated in Figure 2-2 is the use of a calibration curve which converts digital readings from the flow sensor into units of volumetric flow [μL/min]. The calibration curves employed in this research were generated by the author using the process detailed in the next section. Together, the PID controller and calibration curve ensure that a steady stream of fluid is delivered to the microdevice at the desired flow rate. To support the claimed knowledge of these flow rates, the following sections outline the sensor calibration procedure and provide a quantitative analysis of the PID controller performance.

2.1.1.1 Sensor Calibration

The accuracy of flow rates delivered to the device by the pumping system is dependent upon the quality of calibration curves used to calculate volumetric flow rates from digital flow sensor signals. The calibration curves employed during this research were generated by actuating the piston pumps "open-loop" such that the linear displacement rate of the piston is equal to the volumetric flow rate of a calibration point divided by the cross-sectional area of the piston. This process was repeated for a series of flow rates which encompass the flow rates used within the measurement process. The resulting data, relating digital sensor outputs to volumetric flow rate, were then fit with a second-order polynomial which allows proportional, integral, and derivative gains to be calculated for all sensor readings encountered during operation of the pumping system.

2.1.1.2 Calibration Accuracy

The piston diameter of V-series pumps are held to a (0.0001-inch) tolerance. For each of the four piston diameters within the V-series, that equates to less than (±0.25%) deviation from nominal for the cross-sectional area. Therefore, the calibration curve obtained through open-loop displacement of the pistons should fall within one-percent of the expected values; a suitable level of accuracy to support the work performed henceforth.

2.1.1.3 PID-Control Tuning

The transport processes investigated in this research require steady flow conditions. To satisfy this requirement, the PID controller for each of the four pump assemblies was tuned to achieve minimal steady-state oscillation. Additionally, minimization of settling time, or the time to reach steady state, was desired as delays in steadying of flow rates would hinder characterization of transient phenomena. Table 1 provides a breakdown of PID performance for each pump at the flow rates found within this research. In all cases, steady-state oscillation is within a ±2% margin and settling time is less than (5[s]).

Table 1. Summary of PID performance at key volumetric flow rates

Pump (by fluid)	Flow Rate [μL/min]	S.S. Oscillation	Settling Time
Pusher	1.2	±1.25%	< 5[s]
Pusher	0.4	±1.75%	< 5[s]
Pusher	0.2	±1.75%	< 5[s]
Pusher	0.1	±1.75%	< 5[s]
Sphere	300	±0.2%	< 4[s]
Sphere	40	±0.5%	< 4[s]
Lyse	20	±0.5%	< 2[s]
Sheath	1800	±0.2%	< 3[s]
Sheath	900	±0.2%	< 3[s]

2.1.2 Optical Detection

Quantification of in-device cell transport rates is facilitated by laser excitation of individual cells, projection of optically-significant conical segments of scattered light onto photodiodes, and peak detection of the resulting electronic signals. As cells pass through a device's point of measurement, the optical detection system produces two voltage values (one for each of two conical light segments analyzed) which correspond to the size and complexity of a transiting cell [14]; the use of these signal values are critical to categorization of white blood cell signals. Signal categorization consists of 'clustering' signal populations and classifying members of each cluster based on known scattering properties of cell types. An illustration of signal clustering, provided by the experiment outlined in Chapter 3, is provided in Figure 2-3.

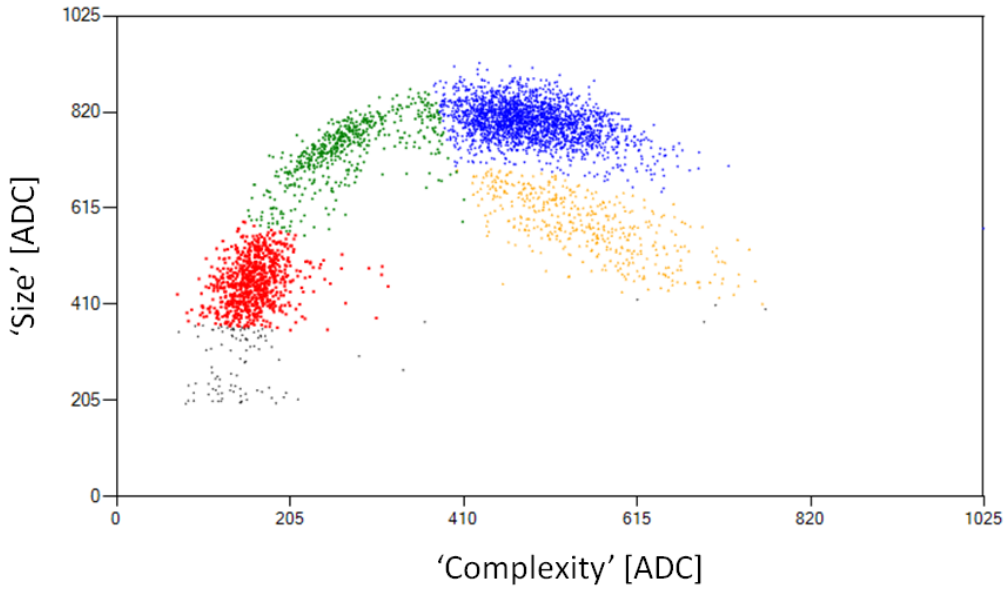

Figure 2-3. Color-coded classification of White Blood Cell subpopulations: Neutrophil (Blue), Lymphocytes (Red), Monocytes (Green), and Eosinophils (Yellow)

The signals shown in Figure 2-3 are the result of a White Blood Cell analysis for which Red Blood Cells were lysed, or made optically non-participating, such that the bulk of collected signals would represent WBCs. After classifying these signals, signals from the target cell type can be grouped by an associated timestamp which is generated for each signal by the detection system. The number of cells within a grouping divided by the timespan of analysis provides the transport rate.

2.2 Microdevice Composition and Functionality

Within this research, the microdevice design is altered for the purposes of experimentation. However, the general architecture of the device will remain constant. In the following sections, this architecture is laid out in terms of the basic device components and the functionality they provide. Parametric details and explanations of differences between the various microdevices are provided in the introduction of the chapters in which they appear. Figure 2-4 provides an overview of the device composition using a representative microdevice. In the figure, labels are provided for the device components which support the three primary measurement processes: cell dispensing, cell processing, and cell focusing.

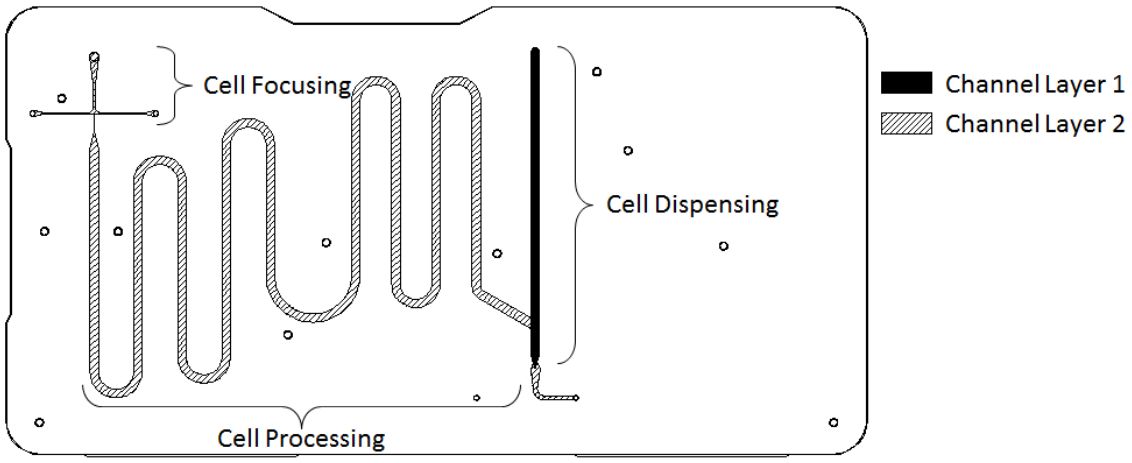

Figure 2-4. Architecture of a microdevice for quantitation of cell concentration in whole blood

2.2.1 Cell Dispensing

The most critical transport process with regard to cell concentration measurement is the controlled transport of blood cells within a whole blood sample which has been loaded into the microdevice prior to the device's insertion into the experimental apparatus (or 'instrument'). In each microdevice, there is a component which facilitates the cell-dispensing process. The cell-dispensing component contains an inlet which is exposed to the external surface of the device. This inlet enables both manual introduction of the blood specimen and introduction of a pusher fluid the device so as to propel the whole blood sample. Additionally, the cell-dispensing component contains an outlet which allows propelled samples to pass into the cell-processing portion of the fluidic circuit.

2.2.2 Cell Processing

Whole blood flowing from the outlet of the cell-dispensing component must be modified with liquid reagents which complement light-scatter detection. Basic reagents fall into

two categories: cell-lysing reagents which destroy RBCs to allow better detection of the less-concentrated WBCs and cell-sphering reagents which, true to name, transform RBCs from their typical discoid shape into spheres and enable determination of cell volume from the intensity of scattered light [15]. Thorough reaction between cells and reagents require both effective mixing (reduction of diffusion length) and suitable dwell time. These parameters are not straightforward design parameters. Rather, the mixing and dwell time are a function of the ratio of whole-blood flow to liquid-reagent flow, the manner in which these flows are combined, and the geometry through which the mixture flows.

In each microdevice, there is a cell-processing component, generally a long channel of fixed cross-section, which facilitates the reaction between whole blood and the liquid reagent. Both the channel and blood-reagent junction are detailed for each device in the introduction of the corresponding chapter. The common features of each cell-processing component are: an inlet which is exposed to the external surface of the device to allow delivery of the processing reagent, a fluidic junction with the cell-dispensing component, and an outlet which leads into the cell-focusing component.

2.2.3 Cell Focusing

The final process to precede signal generation is the hydrodynamic focusing of processed cells. Hydrodynamic focusing refers to the use of bounding fluid streams for alignment of entrained cells. The particular form of cell focusing implemented in each of the

experimental devices involves the use of two streams of ‘sheathing’ fluid to compress the cell-reagent mixture by joining with the mixture at a cross-shaped junction. The volumetric flow rate of the sheath streams, which are significantly greater than that of the mixture, meet with the cell-reagent mixture in such a way that a ‘ribbon’ of cells is formed; the width of this ‘ribbon’ is dictated by the mixture-to-sheath flow rate ratio and is configured to be significantly narrower than the laser beam which is focused on the processed-cell stream. To an extent proportionate to the acceleration of cells passing through this ‘ribbon’, the cell-focusing circuit also enhances cell spacing in the streamwise direction. Both the cell alignment and streamwise spacing of cells facilitated by the focusing component complements the detection process by ensuring cell-to-laser alignment and minimizing the frequency of simultaneous illumination of cells, respectively.

2.3 Measurement Methodology

The first step in the blood sample analysis process is manual injection of whole blood into the cell dispensing feature within the microdevice. With blood loaded into the device, the microdevice is inserted into a mechanical alignment fixture which established a fluidic connection between microdevice fluid inlets and pump system outlets. Additionally, this fixture facilitates alignment of the optical-detection system with the point of detection within the device. After the device is secured by the mechanical alignment fixture, an automated test routine begins.

The composition of an automated routine depends upon the cell concentrations which are of interest; an RBC concentration measurement utilizes a different pumping sequence, processing reagent, and flow rates than a routine for quantifying WBC concentration. The routine used in each experiment is provided in the appropriate overview section. For each routine, there are the primary test segments:

1. Set pump flow rates and allot suitable time for pumps to reach steady state
2. Allot further time for establishing a steady-state transport condition within the cell-processing circuit
3. Cell analysis via optical detection and subsequent calculation of cell transport rate

Steps 1 & 2 of the routine are not altogether distinguishable with regards to the measurement process. Together the steps ensure unity between cell transport rate out of the cell-dispensing circuit and the transport rate which is observed at the point of detection. With this quasi-steady condition established, the detected cell transport rate reflects the 'dispensed' cell transport rate such that the left-hand side of Equation (1-1) becomes known; a claim which is stated more formally in Equation (2-1) wherein, under steady-state conditions, the detected cell transport rate **should** be equal to the product of the pusher fluid volumetric flow rate and the concentration of the detected cell type within the whole blood sample.

$$Desired\ that, @S.S. \qquad \dot{n}_{detected} = c_i * \dot{V}_{pusher\ fluid} \tag{2-1}$$

$$@S.S. \quad \dot{n}_{detected} = \dot{n}_{dispensed} \tag{2-2}$$

As previously stated with regards to Equation (1-1), this research investigates and characterizes conditions which delineate the relationship stated in Equation (2-1) (i.e. Equation (2-1) is shown to be erroneous in many cases). Independently, the equivalence between detected transport rate and dispensed transport rate during the quasi-steady transport state allows for characterization of the cell transport mechanisms taking place within the cell-dispensing component. This equality, expressed in Equation (2-2) provides the basis for quantitative characterization of cell transport within this research. That is—the detected cell transport rates are assumed to reflect the rate of cell transport within (and ultimately out of) the cell dispensing feature of each microdevice. The observed cell transport rates are used to validate hypotheses related the whole blood transport of red and white blood cells within the cell dispensing feature.

Chapter 3: Cell Transport in Vertically-Oriented Whole Blood Microchannel Flows

The experimental investigations detailed in later chapters aim to identify the whole blood phenomena which are pertinent to the transport of red and white blood cells in creeping whole blood microflows. This objective was motivated by the experimental datasets which are presented in this chapter. Given that these data were acquired before the research objective was established, there are no hypotheses toward which the experimentation had been oriented. Rather, the data were obtained as part of a study which compared blood cell concentration measurements obtained with a microdevice to measurements from an FDA-approved, reference instrument. Such studies are commonly used in diagnostics development to gauge and inform the refinement of new technologies. *Post-hoc* analysis of the data from this 'comparison study' shows the microdevice measurements to be in error, yet seemingly-coherent. In Chapter 4, the trends in microdevice measurements are used to generate working hypotheses which merit further investigation.

3.1 Microdevice

The microdevice used in this initial experiment is presented in Figure 3-1. The cell dispensing feature in this device consists of a straight, vertically-oriented (in operation, the normal vector of the device's broad surface is perpendicular to gravity) channel possessing an inlet at its upper end and an outlet located at its lower end. The inlet to the

dispensing channel is exposed to the outer surface of the device while the outlet forms a fluid-fluid juncture with the cell processing channel. The cell-processing channel lies in a separate plane from the cell-dispensing channel. Where the channels intersect, the cell processing channel passes under the cell dispensing channel while a small, cylindrical channel connects the components.

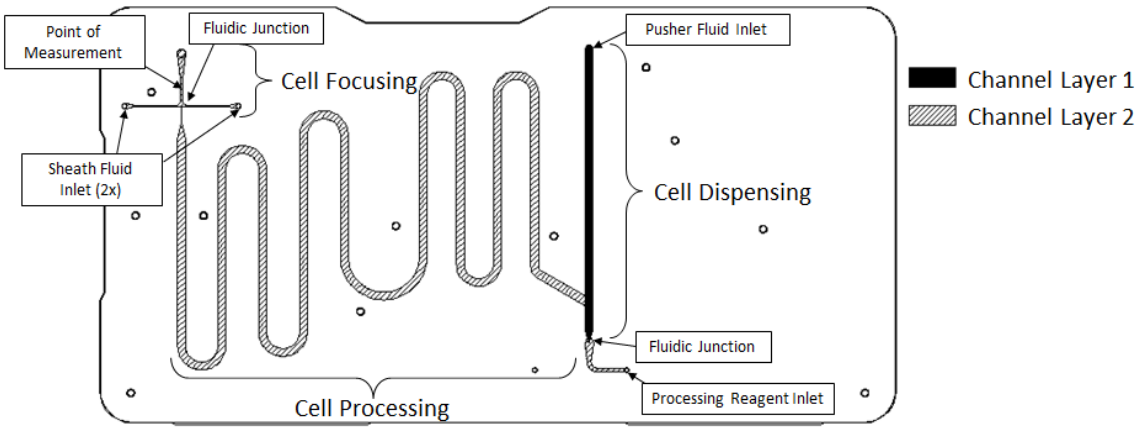

Figure 3-1. Annotated illustration of the microdevice design utilized in the initial comparison study

An isometric view of the juncture between the cell dispensing channel and cell processing channel is provided in Figure 3-2. There, the cell processing channel, cell dispensing channel, and connecting channel are highlighted in dark grey, light grey, and white, respectively. Additionally, flow directionality is indicated for the whole blood, and reagent entering the junction and the cell-reagent mixture exiting the junction.

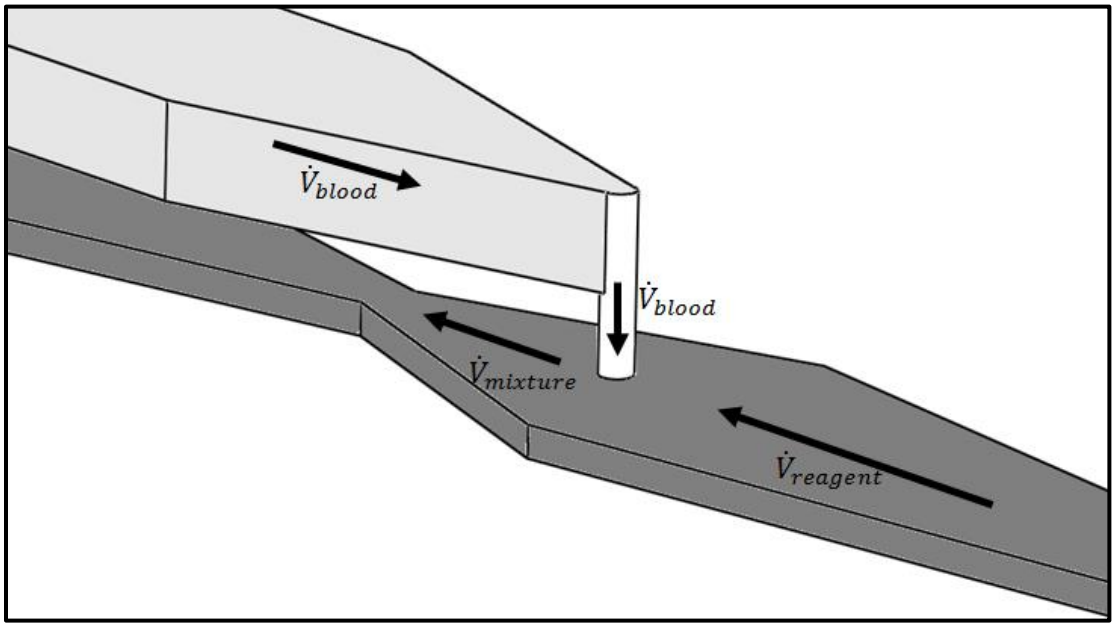

Figure 3-2. Isometric view of fluid-fluid junction between the cell dispensing and cell processing channels within the comparison study device

The cell-reagent mixture which leaves the junction in Figure 3-2 flows onward, through the cell processing channel; the length of which was optimized to ensure thorough reaction of the cells. Ultimately, the cell-reagent mixture arrives at the junction between the cell focusing feature and the cell-processing channel. In this device, the cell-focusing feature and cell-processing channel are co-planar. A schematic of this junction and the manner in which the cell-reagent mixture interacts which the sheath flows is provided in Figure 3-3.

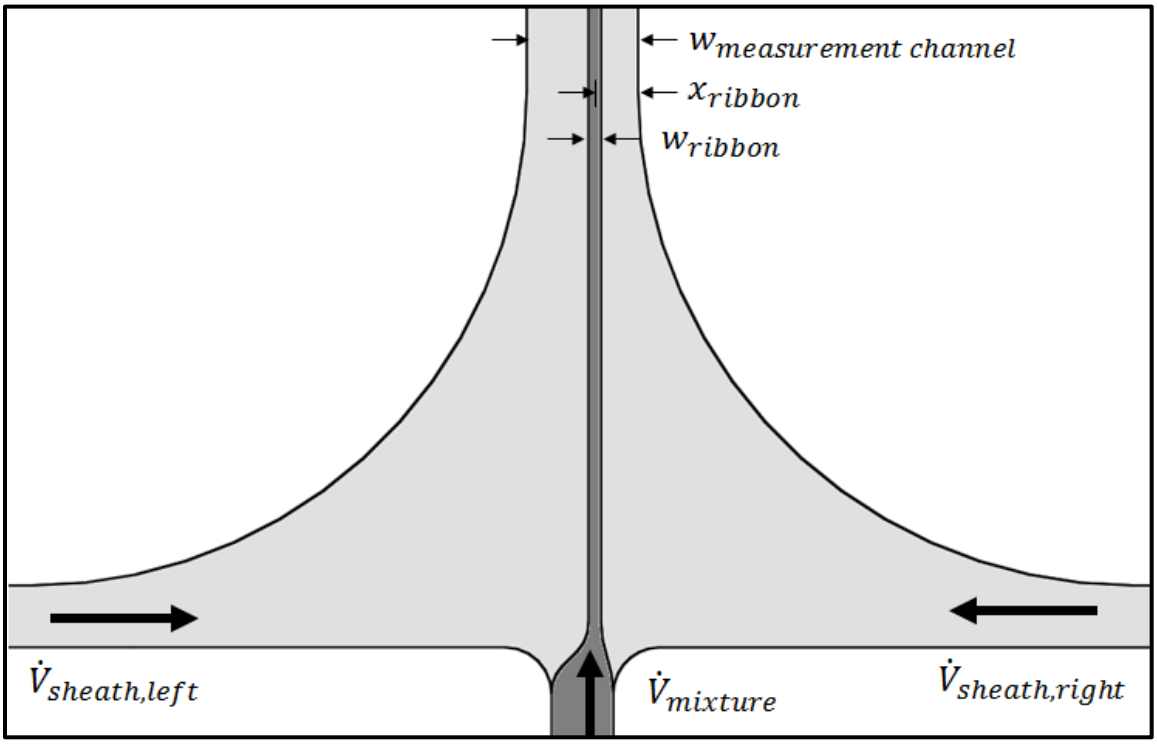

Figure 3-3. Schematic of the cell focusing feature used in each of the experimental devices

Figure 7 does not accurately depict the progression of the cell-reagent-mixture stream through the cell focusing feature. In reality, the width of the stream, previously referred to as the 'ribbon', gradually reduces as it approaches the point of measurement within the 'measurement channel'. Rather than providing a true-to-life illustration of the flow through the measurement feature, Figure 3-3 is intended to aid in establishing the parameters which affect cell focusing in this design. The important properties of the cell ribbon formed by the focusing feature are its width and location within the measurement channel. The width of the ribbon must be small enough to avoid substantial variation in the intensity with which transiting cells are illuminated by the optical-detection system. Additionally, the ribbon must be centrally located within the measurement channel so

that quality optical signals can be obtained which are free from misalignment with the laser illumination and clear of interaction between the detection system's illuminating laser and device's channel edges. Because the flow within the cell focusing feature is low-Reynolds and because the geometry satisfies flat plate conditions, the width (w_{ribbon}) and lateral position (x_{ribbon}) of the cell ribbon can be accurately described with Hele-Shaw descriptions. The equations for ribbon width and lateral position are given in Equation (3-1) and Equation (3-2), respectively.

$$w_{ribbon} = w_{measurement\ channel} * \left(\frac{\dot{V}_{mixture}}{\dot{V}_{sheath,right} + \dot{V}_{sheath,left} + \dot{V}_{mixture}}\right) \quad (3\text{-}1)$$

$$x_{ribbon} \approx w_{ribbon} * \left(\frac{\dot{V}_{sheath,right}}{\dot{V}_{sheath,right} + \dot{V}_{sheath,left}}\right) \quad (3\text{-}2)$$

In Equation (3-1), the width of the ribbon is stated to be equal to the width of the measurement channel multiplied by the ratio of the volumetric flow rate of the cell-reagent mixture to the total volumetric flow rate through the measurement channel. This description is primarily rooted in the conservation of mass; presuming that the flow profile is consistent over a majority of the channel's span such that volumetric transport of each fluid can be assumed proportionate to the width that fluid occupies. Equation (3-2) is an approximation which assumes that the mixture flow rate is significantly less than the bounding flows and states that the ribbon will be positioned a distance from the right channel wall which is equal to the ratio of the right sheath's volumetric flow rate divided by the total sheath volumetric flow rate. In situations where the mixture flow rate is

substantial, the ribbon's centerline location would be offset from that predicted by Equation (3-2) by the ribbon's half width.

3.2 Measurement Routine

For the data sets provided in the Results section of this chapter, red and white blood cell concentration measurements were generated using two separate measurement routines. In reality, each of the two measurement routines provided measurements of both RBC and WBC concentration with the primary difference between the two being the order in which the measurements were taken. For routine 3A, red blood cell concentration was measured first, followed by a measurement of white blood cell concentration. In routine 3B, the order is reversed with white blood cell measurement preceding red blood cell measurement.

Analysis of the datasets from routines 3A and 3B found a strong relationship between the WBC concentration measurements from routine 3A with the RBC concentration measurements from routine 3B. Detailed analysis of this relationship is provided in Chapter 5. Meanwhile, WBC concentration measurements from routine 3B and RBC concentration measurements from routine 3A were either consistent with the reference instrument or showed a substantially-lesser deviation from the reference measurement than in the opposite routine. This finding was taken to imply that the source in device-measurement error stemmed from transient phenomena (i.e. the transport might initially

be well-behaved before skewing from expected) and was an initial clue as to the dominate mechanism affecting microdevice measurements.

Details for measurement routines 3A and 3B are provided in Appendix B. The results presented in this chapter consist of data from the latter measurement of each routine. In other words, the reported RBC concentration measurements correspond to measurement routine 3B while the reported WBC concentration measurements correspond to measurement routine 3A. With that, it should be noted that the reported measurements were taken at nearly-identical time points from one another. Conveniently, this lends credence to the hypotheses derived from the data because the RBC and WBC measurements can be treated as temporally concurrent.

3.2.1 Additional Fluidic Technique for RBC Measurement

The RBC-measurement routine used within the comparison study differs significantly both from the routines of other experiments and the measurement methodology outlined in Chapter 2. Specifically, the RBC measurement routine includes an additional fluidic step which follows the establishment of steady transport within the cell processing channel but precedes RBC measurement. During this extra step, the volumetric flow rate of the cell-processing reagent is set to zero. As a result, the cell-fluid mixture in the cell processing channel undergoes a large shift in bulk velocity. As a result of this shift, the cell transport rate at the point of detection deviates from that of the initial steady state by the ratio of the initial and final bulk velocities; a relationship expressed in Equation (3-3).

$$\dot{n}_{final} = \dot{n}_{initial} * \left(\frac{\dot{V}_{final}}{\dot{V}_{initial}}\right) \quad (3\text{-}3)$$

This technique was used in the comparison study to overcome the inability of an early version of the optical detection system to detect signals at the rate in which cells transited the point of measurement during the initial transport phase. By scaling the transport rate, the shortcoming of the detection system was overcome while the resulting routine description, given in Equation (3-4), still allowed for back calculation of cell concentration.

$$\dot{n}_{detected} = c_{RBC} * \dot{V}_{pusher\ fluid} * \left(\frac{\dot{V}_{pusher\ fluid}}{\dot{V}_{pusher\ fluid} + \dot{V}_{sphering\ reagent}}\right) \quad (3\text{-}4)$$

3.3 Experimental Procedure

In the comparison study, twenty-two unique blood samples were measured with both the microdevice outlined in Section 3.1 and an Abbott CellDyn 3200—the reference instrument. For each sample, a microdevice measurement was obtained with measurement routine 3B while eleven of the twenty-two samples were analyzed using routine 3A. A test matrix, which includes reference RBC and WBC concentration measurements, is provided in Table 2.

Table 2. Test matrix for the comparison of microdevice and reference instrument measurements

Sample	1	2	3	4	5	6	7	8	9	10	11
Ref. RBC [M/uL]	2.06	3.33	3.55	3.65	3.67	4.01	4.60	4.76	4.86	5.42	6.25
Ref. WBC [k/uL]	3.45	3.71	3.73	3.21	11.60	3.29	10.80	26.20	4.23	7.08	5.11
3A	×	×	×	×	×	×	×	×	×	×	×
3B	✓	✓	✓	✓	✓	✓	✓	✓	✓	✓	✓
Sample	12	13	14	15	16	17	18	19	20	21	22
Ref. RBC [M/uL]	4.47	2.22	3.79	2.46	6.29	3.21	1.98	4.05	2.80	3.04	3.82
Ref. WBC [k/uL]	6.14	23.00	3.07	12.40	0.96	5.06	3.90	12.50	8.94	18.20	7.80
3A	✓	✓	✓	✓	✓	✓	✓	✓	✓	✓	✓
3B	✓	✓	✓	✓	✓	✓	✓	✓	✓	✓	✓

3.4 Results

3.4.1 RBC Concentration Measurements

The RBC concentration of each sample was measured using both the microdevice and reference instrument. The reference instrument provides a standard against which the accuracy of device measurements can be gauged. A datum for each sample is provided in Figure 3-4 which shows a strong correlation between microdevice and reference-instrument RBC-concentration measurements.

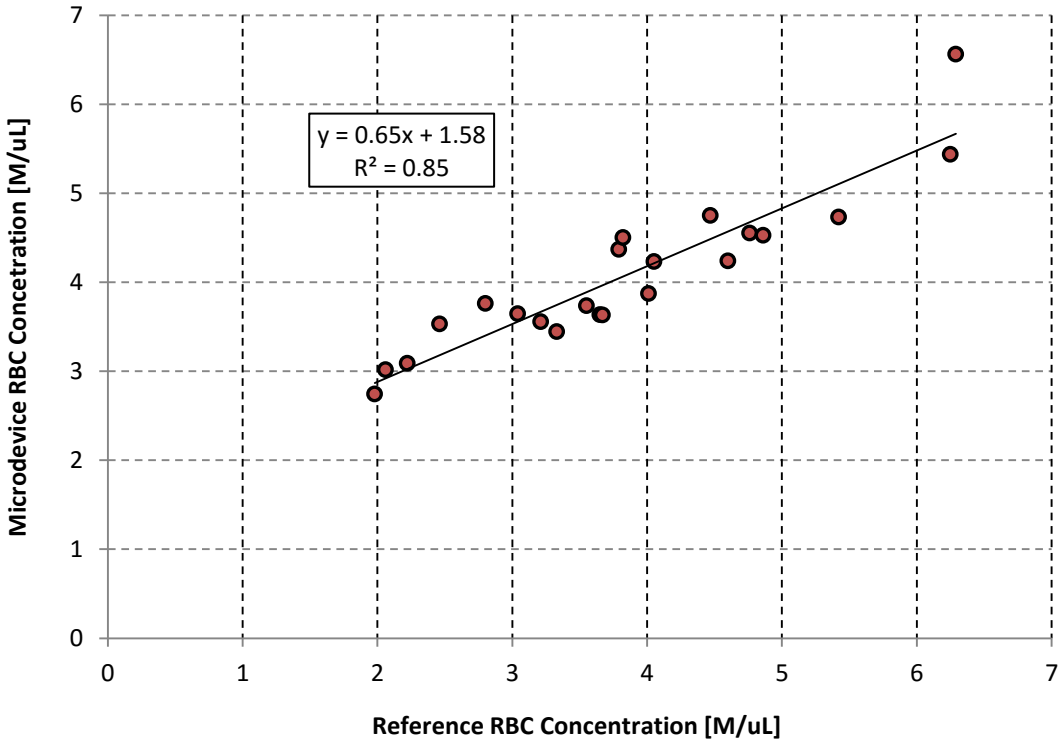

Figure 3-4. Scatterplot illustrating the correlation between microdevice and reference instrument measurements of RBC concentration

3.4.2 WBC Measurements

The WBC concentration of samples (12-22) was measured using both the microdevice and reference instrument. As with the RBC concentration measurements, the reference instrument allows the accuracy of microdevice WBC-concentration measurements to be quantitatively analyzed. A correlation between the microdevice and reference WBC-concentration measurements is provided in Figure 3-5. Again, the correlation between microdevice and reference measurements is strong.

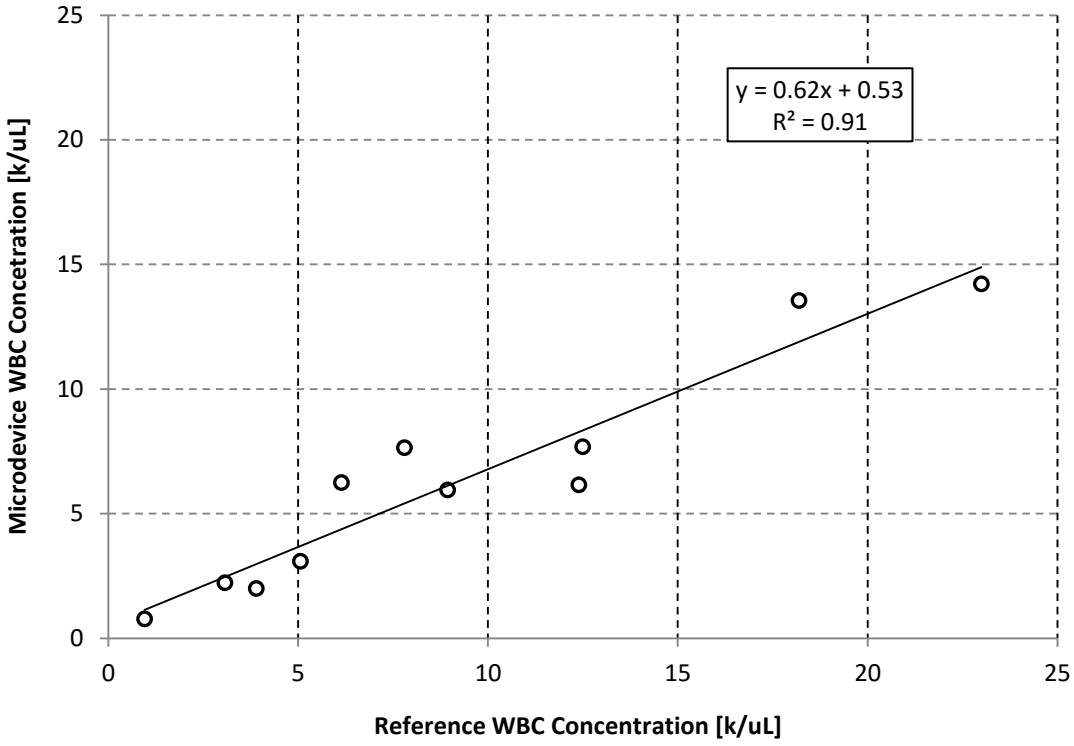

Figure 3-5. Scatterplot illustrating the correlation between microdevice and reference instrument measurements of WBC concentration

Chapter 4: Cell Transport in Sedimenting Whole Blood

Although the correlation plots presented in Chapter 3 validate the fundamental microdevice functionality, data contained therein are not representative of a clinically-viable diagnostic technology. At a minimum, a clinically-viable device must correlate to a reference instrument with a slope near one and intercept near zero such that measurements from the device can be treated as substantially-equivalent to its predecessor. From a technical perspective, the non-unity slopes are particularly concerning given that the working principle of the microdevice, given in Equation (1-1), indicates that direct inference of cell concentrations should be achieved by the microdevice. In other words, a lack of unity between microdevice and reference-instrument measurements implies that the physical operation of the microdevice deviates significantly from the ideal case around which its functionality is derived.

4.1 A Link between Microdevice-Measurement Bias and Whole Blood Composition

Scrutiny of the data from Chapter 3 would eventually yield a set of hypotheses aimed at explaining the deviation of microdevice measurements from those of the reference instrument. The extent of that deviation plays a key role in the formulation and validation of said hypotheses and is regularly referred to as a measurement's bias. Within the context of this research, bias refers to the fractional difference of a microdevice measurement from the corresponding reference measurement. The formula

for calculating bias is given in Equation (4-1) in terms of the concentration of cell-type 'i' (either RBC or WBC) as determined by the microdevice $\left(c_{i,microdevice}\right)$ and reference instrument$\left(c_{i,reference}\right)$. The bias of RBC (red-filled circles) and WBC (white-filled circles) measurements from the comparison study are plotted relative to reference RBC concentration in Figure 4-1.

$$Bias = \left(\frac{c_{i,microdevice} - c_{i,reference}}{c_{i,reference}}\right) \quad (4\text{-}1)$$

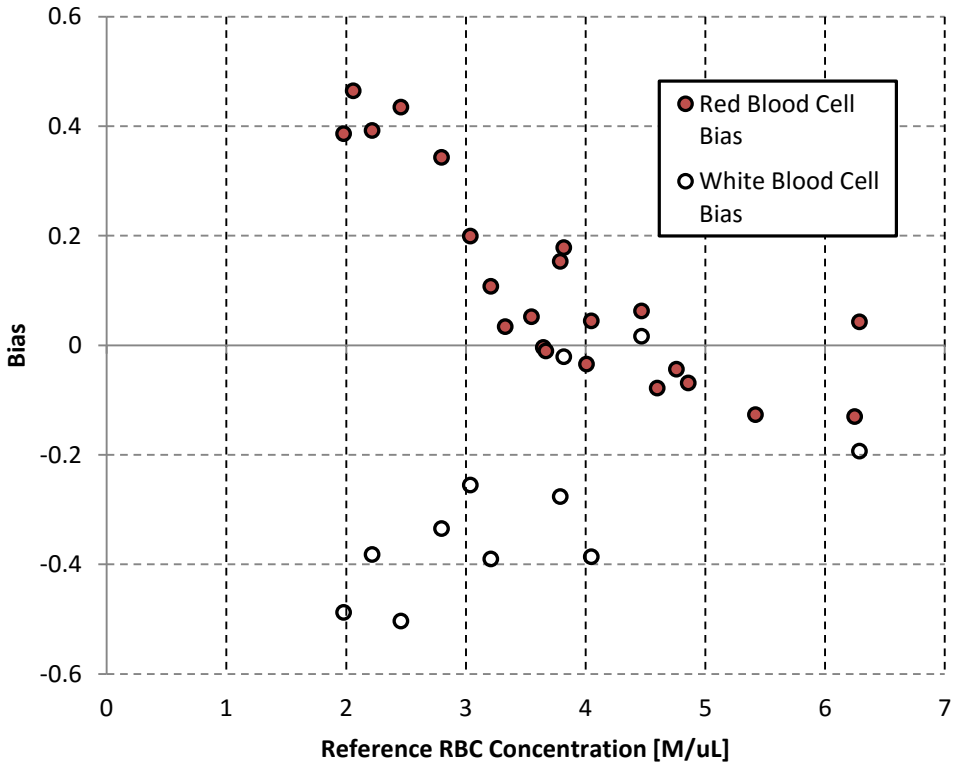

Figure 4-1. RBC and WBC biases for the comparison study data

Figure 4-1 contains a number of important observations regarding the microdevice measurements from the comparison study. First, it indicates that the magnitude of bias is

strongly tied to the sample's RBC concentration: samples with high RBC concentration measured closer to reference than samples with lower concentration. The plot also suggests that dominant bias sources affect RBCs and WBCs oppositely; resulting in an inversely-proportionate deviation from reference at lower RBC concentrations. Because measurement bias appeared to be dependent upon a sample's composition, it was theorized that sample measurements were influenced by whole blood phenomena. Additionally, the relationship between measurement bias and the sample's RBC concentration suggested that the primary biasing phenomenon was itself a function of RBC concentration.

4.2 A Working Hypothesis for Microdevice-Measurement Bias

In considering possible causes of the bias illustrated in Figure 4-1, it was important that proposed theories agree with each of four key observations pertaining to that data. These observations were:

- Bias magnitude is strongly related to RBC concentration
- RBCs and WBCs are affected oppositely; relatively equally
- The bias-causing mechanism is likely a time-dependent phenomena
- All samples follow a similar trend

While the first three observations reveal something of the nature of the bias-causing mechanism, the fourth observation is equally important in that it suggests that device-measurement bias is the product of a common blood property rather than a physiological condition (illness). Given that, a hypothesis might be extracted from research of

fundamental whole blood research as opposed to linking device bias with a whole blood abnormality. Acting upon that notion, a review of whole blood flows was conducted; focusing primarily on the Hemorheology literature compiled in [16]. Among the phenomena laid out in that text, erythrocyte sedimentation seemed an especially-likely cause of device-measurement bias.

4.2.1 Erythrocyte Sedimentation

Erythrocyte (read: red blood cell) sedimentation is an innate whole blood phenomenon in which the RBCs in a static volume of whole blood settle out of suspension. This is a well-studied phenomenon due in part to its use as a general screen for illness [17] in the form of an erythrocyte sedimentation rate (ESR) test. An ESR test is conducted by injecting whole blood into a graduated glass tube having a (2.55[mm]) internal diameter [18]. The tube is then oriented such that the tube axis is aligned with gravity. Estimation of the ESR is then obtained by recording the position of the interface between the red-cell-containing volume and RBC-free plasma region which forms at the top of the tube at regular time intervals spanning the desired window of observation.

In [19], high-resolution ESR recordings show the rate of interface advancement to be time-dependent. Initially, the interface proceeds slowly (or not at all) while increasing in rapidity. Eventually, this acceleration gives way to a period of constant interface motion. As the interface approaches the region of packed cells near the bottom of the tube, the rate of interface progress slows and eventually ceases when the cells reach a fully-packed

condition. The author of [19] illustrates these 'phases' with a time plot of interface location; provided in Figure 4-2.

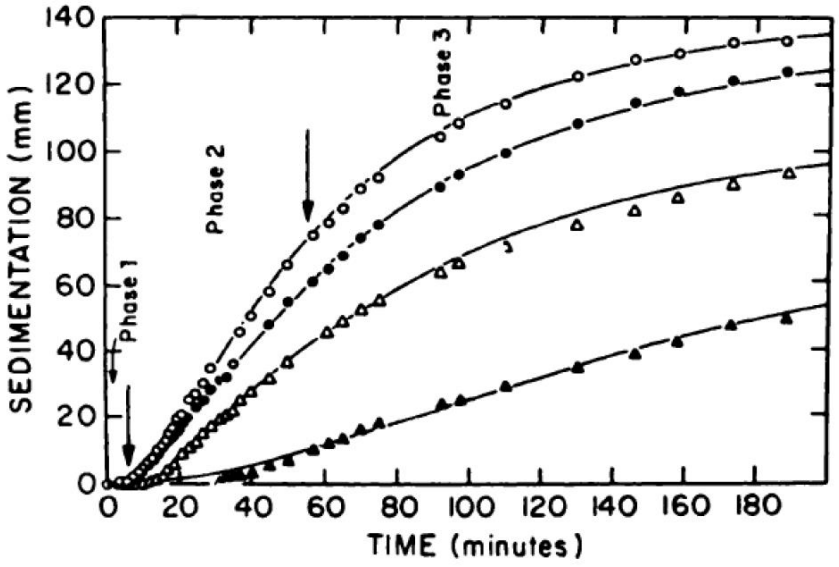

Figure 4-2. From [19]: Cell-plasma interface location as a function of time for various hematocrit (HCT) values (from left to right: HCT = 26, 28, 34, 45)

The data presented in Figure 4-2 is doubly supportive of RBC sedimentation as the primary bias-causing mechanism. First of all, it shows the magnitude of RBC sedimentation to be time-dependent. This is perhaps why device-measurement bias is more pronounced in measurements taken later in the course of routines. Secondly, the author shows a consistent trend between hematocrit (HCT) and the sedimentation rate of a sample. Assuming a rough equivalence between HCT and RBC concentration, this data confirms an increase in ESR with decreasing RBC concentration which again agrees with the observations from the comparison study.

One facet of the comparison study data not yet addressed is the effect of RBC sedimentation upon WBCs. The device-measurement bias from the comparison study suggests that the primary bias-causing mechanism should affect WBCs in a manner opposite to RBCs. In a case where that mechanism is RBC sedimentation, this implies a counter-settling of white blood cells. Such a phenomenon is covered in [20] where the concentration of RBCs and WBCs in the upper half of a sedimentation tube was measured after varying durations of sedimentation. The authors use these measurements to determine the rate at which WBCs transport along-with or counter-to RBCs during sedimentation. Their findings showed that while sedimentation depleted RBCs from the upper half of tubes, the WBC concentration in that segment would rise. Furthermore, the authors concluded that the rate of RBC depletion was "similar" to the rate of leukocyte anti-sedimentation, or 'flotation'.

4.3 The Effect of Erythrocyte Sedimentation upon the Rate of Cell Dispensing

Further evidence supporting erythrocyte sedimentation as the dominant bias mechanism came from [21] wherein a population study was conducted which focused on the Erythrocyte Sedimentation Rate (ESR) of sickle-cell and 'normal' blood samples. Plots from this publication, one of which is shown in Figure 4-3, illustrate the relationship between ESR and a patient's hematocrit (solid volume fraction of blood). The ESR data for 'normal' samples (bounded in grey) show a trend between ESR and hematocrit

similar to the trend between RBC bias and sample RBC concentration: ESR increases as the solid volume fraction of blood decreases.

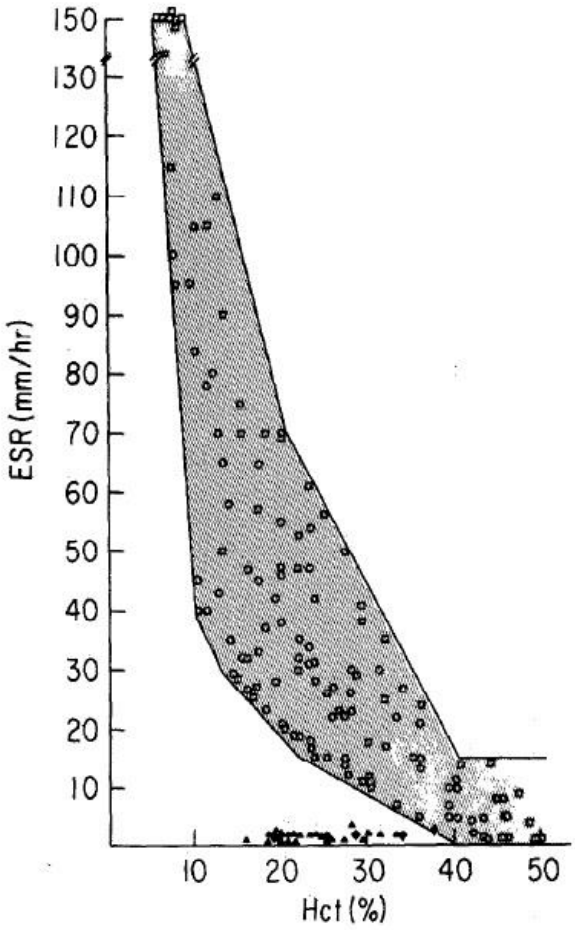

Figure 4-3. From [21]; Plot of ESR values for sickle-cell (diamond) and healthy (circle) samples

4.3.1 Microdevice Bias as a Function of ESR

The trend in ESR relative to HCT, shown in Figure 4-3, resembled the RBC bias trend in Figure 4-1 to such an extent that an effort was made to tie a mathematical connection between the two. The derivation begins by assuming that RBCs in the cell dispensing channel transit at a speed equal to the bulk flow velocity plus the ESR of a given sample; expressed mathematically in Equation (4-2).

$$\bar{u}_{RBC} \approx \bar{u}_{bulk} + ESR \tag{4-2}$$

In order to relate the kinematic impact of ESR to the transport of cells in the cell-dispensing channel, a relationship between channel-wise cell velocity and cell transport was established in Equation (A-6) (see Appendix A for derivation). For the purposes of describing the impact of ESR upon RBC transport, Equation (A-6) can be rewritten as in Equation (4-3) where the rate of cell transport along the cell dispensing channel is stated as the product of the number of cells (N) bounded by a control volume (which spans the entire channel cross-section) and the average channel-wise velocity $(\bar{u}_{\vec{s}})$ of bounded cells, divided by the channel-wise length (Δs) of said control volume.

$$\dot{n} = \frac{N * \bar{u}_{\vec{s}}}{\Delta s} \tag{4-3}$$

The RBC velocity approximation from Equation (4-2) can be substituted for the average stream-wise velocity term in Equation (4-3). The resulting expression, Equation (4-4) describes the expected RBC transport for a sedimenting whole blood flow.

$$\dot{n}_{RBC} = \frac{N * (\bar{u}_{bulk} + ESR)}{\Delta s} \tag{4-4}$$

In order to relate this description of RBC transport to the observed RBC bias, Equation (4-1) should be rewritten with the microdevice-measured RBC concentration replaced by the detected-RBC rate $\left(\dot{n}_{RBC,detected}\right)$ divided by the volumetric flow rate of the pusher fluid$\left(\dot{V}_{pusher\ fluid}\right)$; the formula used to calculate microdevice measurements.

$$Bias_{RBC} = \frac{\left(\frac{\dot{n}_{RBC,detected}}{\dot{V}_{pusher\ fluid}}\right)}{c_{RBC,reference}} - 1 \tag{4-5}$$

An equation for the relationship between the expected RBC-measurement bias of a sedimentation-influenced measurement can then be obtained by substituting the right-hand side of Equation (4-4) for the detected-RBC rate $\left(\dot{n}_{RBC,detected}\right)$ in Equation (4-5); yielding Equation (4-6).

$$Bias_{RBC,expected} = \frac{\frac{N_{RBC} * (\bar{u}_{bulk} + ESR)}{\Delta s}}{\dot{V}_{pusher\ fluid} * c_{RBC,reference}} - 1 \tag{4-6}$$

Equation (4-6) can be simplified by expanding the terms in the ratio's denominator using the appropriate terms present in the numerator. The equalities used to make this expansion are provided in Equations (4-8) and (4-9) while the expanded form is given in Equation (4-7).

$$Bias_{RBC,expected} = \frac{\frac{N_{RBC} * (\bar{u}_{bulk} + ESR)}{\Delta s}}{\left(\frac{N_{RBC}}{A_c * \Delta s}\right) * \bar{u}_{bulk} * A_c} - 1 \tag{4-7}$$

$$\dot{V}_{pusher\ fluid} = \bar{u}_{pusher\ fluid} * A_c = \bar{u}_{bulk} * A_c \quad (4\text{-}8)$$

$$c_{RBC,reference} = \left(\frac{N_{RBC}}{A_c * \Delta s}\right) \quad (4\text{-}9)$$

Cancellation of terms in Equation (4-7) reveals a simple relationship between the predicted RBC-measurement bias and the ESR of a blood sample. This relationship, given in Equation (4-10) states that the bias of ESR-affected measurements should be equivalent to the sample's ESR divided by the bulk flow velocity within the cell dispensing channel.

$$Bias_{RBC,expected} = \frac{ESR}{\bar{u}_{bulk}} \quad (4\text{-}10)$$

4.3.2 Inferring ESR Values from Device-Measurement Bias

If the biases of device measurements within the comparison study were the product of erythrocyte sedimentation, the data in Figure 4-1 should reflect the relationship in Equation (4-10). Though the ESR for each sample is unknown, both the bulk blood flow velocity and measurement biases are known. A simple rearrangement of Equation (4-10) yields Equation (4-11) which states that an ESR value can be calculated, or inferred, as the product of RBC-measurement bias and the bulk blood flow velocity.

$$ESR_{inferred} = Bias_{RBC} * \bar{u}_{bulk} \quad (4\text{-}11)$$

The bulk blood flow velocity within the cell dispensing channel is equal to the volumetric flow rate of pusher fluid $\left(\dot{V}_{pusher\ fluid}\right)$ divided by the channel's cross-sectional area(A_c). The substitution of these parameters for the bulk-velocity term in Equation (4-11) yields Equation (4-12).

$$ESR_{inferred} = Bias_{RBC} * \left(\frac{\dot{V}_{pusher\ fluid}}{A_c}\right) \tag{4-12}$$

For the comparison-study microdevice, the cell dispensing channel was (0.3[mm]) deep, and (1.0[mm]) wide while the volumetric flow rate of pusher fluid was (1[mm^3/min]) or (60[mm^3/hr]). Thus, the coefficient relating ESR and RBC bias is (165.3 [mm/hr]) for the comparison study data set. The product of each microdevice-RBC-measurement bias with this coefficient is plotted in Figure 4-4 alongside the bounding-box margins from Figure 4-3.

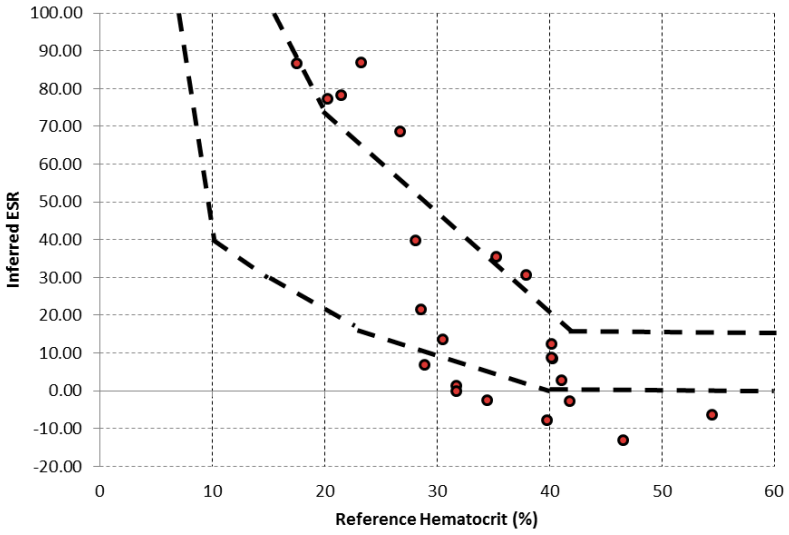

Figure 4-4. Plot of ESR values inferred from the comparison study bias (red-filled circles) with the bounding box from Figure 4-3

The demonstrated agreement between inferred ESR values and the bounding box of ESR values published in [21] further the support for experimental investigation of the effects of RBC sedimentation upon cell transport in the cell dispensing feature. However, prior to formulating a plan to address sedimentation bias, it was important to provide a similar treatment to describing WBC transport in the cell dispensing channel as was given for the transport of RBCs.

4.4 WBC Transport in Sedimenting Whole Blood

Leukocyte flotation, or anti-sedimentation, refers to the upward (opposite gravity) transport of white blood cells in sedimenting whole blood. As the sedimenting body is primarily dominated by red blood cell motion, it should be possible to leverage the previously-developed description of RBC transport to describe the transport of white blood cells. Additionally, if flotation were the dominate mechanism of WBC transport, the microdevice-WBC-measurement biases from the comparison study should agree with this description.

4.4.1 Description of WBC Flotation

The primary assumption of this derivation is that WBCs will flow uninhibitedly within the plasma phase of sedimenting whole blood. As the volume fraction of red blood cells can exceed (50%), this is likely a flawed assumption. However, a description of WBC flotation based on this assumption will enable an initial assessment of WBC transport based on the comparison-study data. Derivation of the WBC-flotation description begins

with a conservation equation, Equation (4-13). It states that the volumetric flow rate of plasma $\left(\dot{V}_{plasma}\right)$ is equal to the bulk volumetric rate $\left(\dot{V}_{bulk}\right)$ through the cell-dispensing channel minus the volumetric flow rate of RBCs, $\left(\dot{V}_{RBC}\right)$. As a note: all flow conditions apply to the WBC-measurement phase of Routine 3A.

$$\dot{V}_{plasma} = \dot{V}_{bulk} - \dot{V}_{RBC} \tag{4-13}$$

Next, the effects of RBC sedimentation must be introduced. The volumetric flow rate of sedimenting RBCs can be stated as the product of the mean cell volume (MCV) and the RBC-transport rate, $(\dot{n}_{RBC})$. This relationship, shown in Equation (4-14), can then be substituted into Equation (4-13) to give Equation (4-15).

$$\dot{V}_{RBC} = MCV * \dot{n}_{RBC} \tag{4-14}$$

$$\dot{V}_{plasma} = \dot{V}_{bulk} - MCV * \dot{n}_{RBC} \tag{4-15}$$

As outlined in the prior sections, it is suspected that the RBC-transport rate deviates from Equation (1-1) by an amount equal to a blood sample's ESR divided by the bulk flow velocity of whole blood within the cell-dispensing channel. Therefore, the RBC-transport-rate term in Equation (4-15) can be replaced with the product of the right-hand side of Equation (1-1) multiplied by a unity scalar which is offset by said ratio. The result of this substitution is given in Equation (4-16) wherein the prescribed formula for RBC-transport rate is bracketed.

$$\dot{V}_{plasma} = \dot{V}_{bulk} - MCV * \left[c_{RBC} * \dot{V}_{bulk} * \left(1 + \frac{ESR}{\bar{u}_{bulk}}\right)\right] \tag{4-16}$$

At this point, the derivation diverts in order to modify the focus of Equation (4-16). Whereas this equation describes the volumetric flow rate of plasma, what is desired is a description of expected WBC-measurement bias based on known quantities. This shift begins with the WBC-analog of Equation (4-3): Equation (4-17). Equation (4-17) states that the WBC-transport rate within a straight channel of uniform cross section (here, the cell-dispensing channel) can be calculated as the product of the total number (N) and average channel-wise velocity $\left(\bar{u}_{\vec{s},WBC}\right)$ of WBCs bounded by a control volume divided by the channel-wise length (Δs) of said volume.

$$\dot{n}_{WBC} = \frac{N * \bar{u}_{\vec{s},WBC}}{\Delta s} \tag{4-17}$$

The assumption of uninhibited WBC transport allows channel-wise WBC velocity to be replaced with a plasma velocity $\left(\bar{u}_{plasma}\right)$ term. In turn, the plasma velocity term can be substituted by the volumetric flow rate of plasma $\left(\dot{V}_{plasma}\right)$ divided by the fluid-fraction of the channel's cross-sectional area; calculated as the complement of hematocrit (HCT') multiplied by the channel area (A_c). The result of these substitutions is given in Equation (4-18).

$$\dot{n}_{WBC} = \frac{N * \left(\frac{\dot{V}_{plasma}}{A_c * HCT'}\right)}{\Delta s} \tag{4-18}$$

Equation (4-18) can be reduced to a simpler form by combining (N), (Δs), and (A_c) to yield a WBC-concentration term (c_{WBC}). In turn, the $\left(\dot{V}_{plasma}\right)$ term can be isolated to

give Equation (4-19). Subsequently, Equation (4-19) can be substituted into Equation (4-16) to give Equation (4-20).

$$\dot{V}_{plasma} = \frac{\dot{n}_{WBC} * HCT'}{c_{WBC}} \tag{4-19}$$

$$\frac{\dot{n}_{WBC} * HCT'}{c_{WBC}} = \dot{V}_{bulk} - MCV * \left[c_{RBC} * \dot{V}_{bulk} * \left(1 + \frac{ESR}{\bar{u}_{bulk}}\right)\right] \tag{4-20}$$

Distributing the WBC-concentration and hematocrit-complement terms in Equation (4-20) gives way to Equation (4-21). Furthermore, dividing both sides of Equation (4-21) by the ideal WBC-transport rate $\left(\dot{n}_{WBC,ideal} \; or \; c_{WBC} * \dot{V}_{bulk}\right)$ yields Equation (4-22). The WBC-concentration and bulk volumetric flow rate terms in the right-hand side of Equation (4-22) cancel. Additionally, the mean-cell-volume, and RBC-concentration terms can be replaced with a hematocrit (HCT) term.

$$\dot{n}_{WBC} = \frac{c_{WBC}\left\{\dot{V}_{bulk} - MCV * \left[c_{RBC} * \dot{V}_{bulk} * \left(1 + \frac{ESR}{\bar{u}_{bulk}}\right)\right]\right\}}{HCT'} \tag{4-21}$$

$$\left(\frac{\dot{n}_{WBC}}{\dot{n}_{WBC,ideal}}\right) = \frac{c_{WBC}\left\{\dot{V}_{bulk} - MCV * \left[c_{RBC} * \dot{V}_{bulk} * \left(1 + \frac{ESR}{\bar{u}_{bulk}}\right)\right]\right\}}{c_{WBC} * \dot{V}_{bulk} * HCT'} \tag{4-22}$$

$$\left(\frac{\dot{n}_{WBC}}{\dot{n}_{WBC,ideal}}\right) = \frac{\left\{1 - \left[HCT * \left(1 + \frac{ESR}{\bar{u}_{bulk}}\right)\right]\right\}}{HCT'} \tag{4-23}$$

Because microdevice measurements are linearly related to the WBC-transport rate, the ratio of actual to ideal WBC-transport rate is equal to the ratio of actual to ideal microdevice measurements. Therefore, Equation (4-23) can be rewritten as a description

of WBC-measurement bias simply by subtracting (1) from its right-hand side. This relationship is given in Equation (4-24).

$$Bias_{WBC} = \frac{\left\{1 - \left[HCT * \left(1 + \frac{ESR}{\bar{u}_{bulk}}\right)\right]\right\}}{HCT'} - 1 \tag{4-24}$$

Subsequent cancellation of terms simplifies the expression, resulting in Equation (4-25).

$$Bias_{WBC} = -\frac{HCT * \left(\frac{ESR}{\bar{u}_{bulk}}\right)}{1 - HCT} \tag{4-25}$$

4.4.2 Comparison of WBC-Measurement Bias with Flotation Model

In Section 4.2.2, RBC-measurement biases were used to infer ESR values for the samples analyzed during the comparison study. In turn, these inferred-ESR values can be used to calculate an expected WBC-measurement bias using Equation (4-25). Both the inferred-ESR and hematocrit (HCT) values in this expression are sample-dependent parameters with the latter being provided by the reference instrument. The bulk velocity is a fixed quantity calculated as the bulk volumetric flow rate of blood during the WBC-measurement phase of routine 3A divided by the cell-dispensing channel's cross-sectional area. The calculated bias data are plotted in Figure 4-5 alongside the measured bias data from the comparison study.

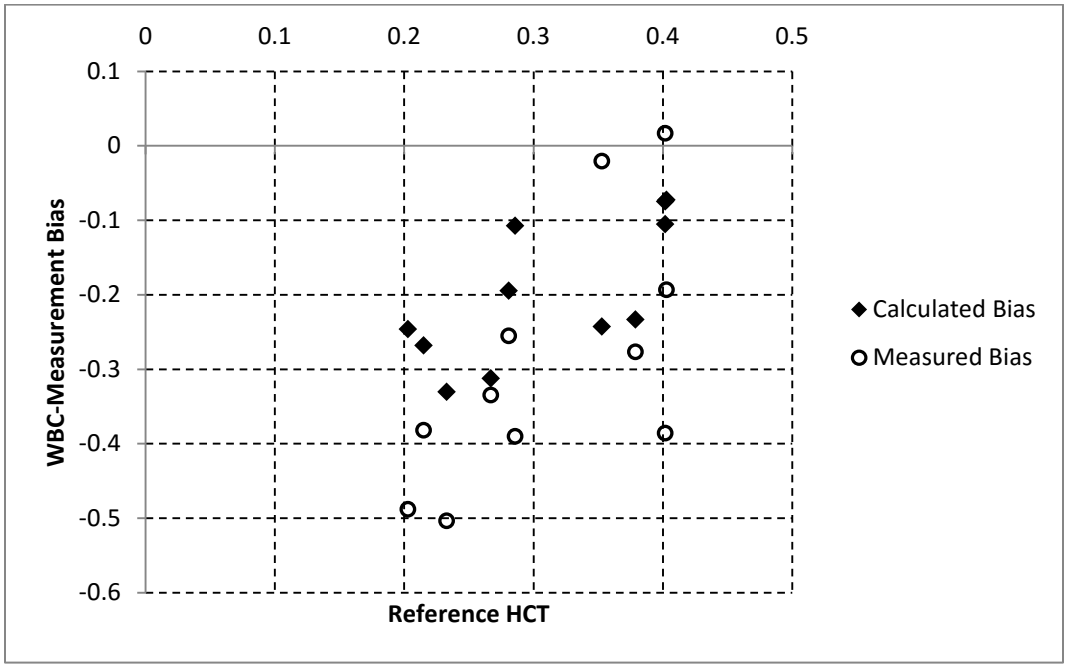

Figure 4-5. Plot of calculated and measured WBC-measurement bias (from comparison study)

The calculated-bias data (black diamonds) in Figure 4-5 demonstrate a trend that resembles that of the actual measurement bias (white circles) in that each dataset shows increasingly-negative bias as the hematocrit of measured samples decreases. However, it is not reasonable to claim good general agreement between the calculated and measured bias. The disagreement between the sets could stem from any number of causes though it is important to note that the measured bias often exceeds the calculated bias. If the assumption of uninhibited WBC flotation were the cause of discrepancy, the opposite would be expected. Given that, there are two possible categories of issue with the analysis used to generate Figure 4-5.

One possible flaw in the post-hoc analysis of the comparison study data lies in the physical separation of observations of RBC and WBC transport. Optimally, measurement of transport rates for the two cell types would occur simultaneously. As the data sets for RBCs and WBCs have, to this point, been generated using separate test routines, the flow conditions pertaining to them are not identical. Consider, for instance, that the flow rate through the cell-dispensing channel may alter the sedimentation rate of RBCs. Under such circumstance, the application of ESR values extracted from RBC-measurement conditions cannot be validly applied to a description of WBC transport.

The second issue to be considered is the potential for additional phenomena affecting RBC and or WBC transport. The following chapter details two phenomena which would have likely played a role in the cell-dispense rates within the initial microdevice.

Chapter 5: Pertinent Phenomena for Cell Transport in Whole Blood Microflows

5.1 Effects of Device Loading

A major misgiving with regard to prior descriptions of cell transport is the assumption that blood occupying the cell-dispensing channel is unaltered at the beginning of a measurement routine. It is important to recognize that initiation of a test routine is preceded by a potentially-significant transport process: device loading. In order to establish the technical significance of device loading, a 'proper' load is defined as the establishment of a steady transport within the cell-dispensing channel. Assume that the vessel (e.g. a large-bore pipette) which facilitates sample loading ensures unity between the injected cell transport rate $\left(\dot{n}_{loading}\right)$ and the product of outlet bulk flow rate$\left(\dot{V}_{loading}\right)$, and reference cell concentration$\left(c_{i,ref}\right)$, stated formally in Equation (5-1).

$$\dot{n}_{loading} = c_{i,ref} * \dot{V}_{loading} \tag{5-1}$$

Again adopting Equation (4-3), the loading-phase transport rate can be treated as the product of channel-wise linear cell concentrations $\left(\frac{N}{\Delta s}\right)$ and average channel-wise cell velocity $(\bar{u}_{\tilde{s}})$ within the cell-dispensing channel; Equation (5-2). Here, it is important to consider the cell-dispensing channel as a succession of control volumes between which the channel-wise concentration and average channel-wise velocity may vary. Yet, by the definition of a proper load, these variables must satisfy Equation (5-2) at the conclusion of the loading process.

$$\left(\frac{N_i}{\Delta s} * \bar{u}_{i,\vec{s}}\right)_{c.v.} = c_{i,ref} * \dot{V}_{loading} \tag{5-2}$$

As blood flows through the cell-dispensing channel during loading, the mechanics of blood flow can alter the distribution of cells within the cross-section of the channel. The mechanics of the alteration are not the immediate focus. However, the consequences of redistribution can be explained by one example: leukocyte margination, here. Leukocyte (WBC) margination is a phenomenon linked with hemodynamic and rheological mechanisms which displace WBCs within the cross-section of a whole blood capillary flow [22]. In terms of the device-loading process, the redistribution of WBCs is of concern because of the relationship between cross-sectional position and channel-wise velocity. More to the point, satisfaction of Equation (2-1) requires a specific relationship between loading-phase and dispensing-phase cell motion. To show this relationship, an analysis will be performed for one of the control volumes occupying the cell-dispensing channel. For this control volume, the ideal dispensing-phase cell transport rate is given by Equation (2-1) which can be rewritten in the form of Equation (5-2) as Equation (5-3).

$$\frac{N_i}{\Delta s} * \bar{u}_{i,\vec{s},dispensing} = c_{i,ref} * \dot{V}_{dispensing} \tag{5-3}$$

Assuming the distribution of cells within the channel is constant between the end of the loading and beginning of the dispensing phase, $\left(\frac{N_i}{\Delta s}\right)$ terms can be treated as equal and Equations (5-2) & (5-3) can be combined to form Equation (5-4).

$$\frac{\dot{V}_{loading}}{\dot{V}_{dispensing}} = \frac{\bar{u}_{i,\vec{s},loading}}{\bar{u}_{i,\vec{s},dispensing}} \tag{5-4}$$

Equation (5-4) states a necessary condition for the relevance of Equation (2-1): the ratio of average cell velocity must be proportionate to the ratio of bulk volumetric flow rate when comparing the loading and dispensing phases. This condition is innately true of molecules transported in homogeneous solutions; a process which is often given descriptions similar to Equation (2-1). However, whole blood is a mixture for which Equation (5-4) is only conditionally applicable. With non-uniform WBC distributions for instance, Equation (5-4) would be necessarily satisfied if the normalized velocity profiles for the loading and dispensing transport phases were identical. This would be expected for creeping, Newtonian flow conditions. However, whole blood exhibits non-Newtonian behavior under low shear conditions [23] and a yield stress near stasis [24] [25]. As such, the change in bulk flow rate between device loading and cell dispensing will result in a change in the cross-sectional velocity profile. Consequently, cells do not necessarily experience deceleration which is proportionate to the change in bulk volumetric flow rate. Depending on the extent of cell inhomogeneity, this shift in velocity profile may significantly violate Equation (5-4) and, in turn, invalidate Equation (2-1) as a description of the cell-dispensing process.

5.2 Sedimentation in Shearing Whole Blood

In Chapter 4, erythrocyte sedimentation was shown to be a three-phase process. In the initial phase, progress of the cell-plasma interface is slow but gradually increasing in linear velocity. The cause of this increase in sedimentation rate during the initial, or ‘lag’, phase is the aggregation of red blood cells which increases the permeability of the

blood's solid phase such that a constant gravitational force produces greater upward transport of plasma [26]. For a majority of blood samples, aggregation is a reversible process [27]; aggregates formed under low-shear conditions will disaggregate under elevated shear [28]. The dependence of aggregation upon shear conditions raises questions regarding the previous descriptions of ESR-biased cell transport: how does the presence of shear in the duct flow within the microdevice affect sedimentation?

If sedimentation were strictly proportional to aggregation, it would be sensible to expect that any shear which inhibits aggregation should in turn reduce the rate of sedimentation. Oppositely, in [29], it was shown that the shear-ESR relationship is complex; low shear rates do not affect ESR ($0\text{-}10^{-3}[s^{-1}]$) but increasing levels of shear will lead to an enhancement of ESR ($10^{-3}\text{-}10^{-1}[s^{-1}]$). Beyond a peak sedimentation rate, corresponding to a shear rate of approximately ($10^{-1}[s^{-1}]$), the sedimentation rate begins to reduce and eventually diminishes altogether ($10^{-1}\text{-}10^{1}[s^{-1}]$). This relationship is illustrated in Figure 5-1 which contains experimental data for ESR of whole blood samples of varying hematocrit under an array of shear conditions.

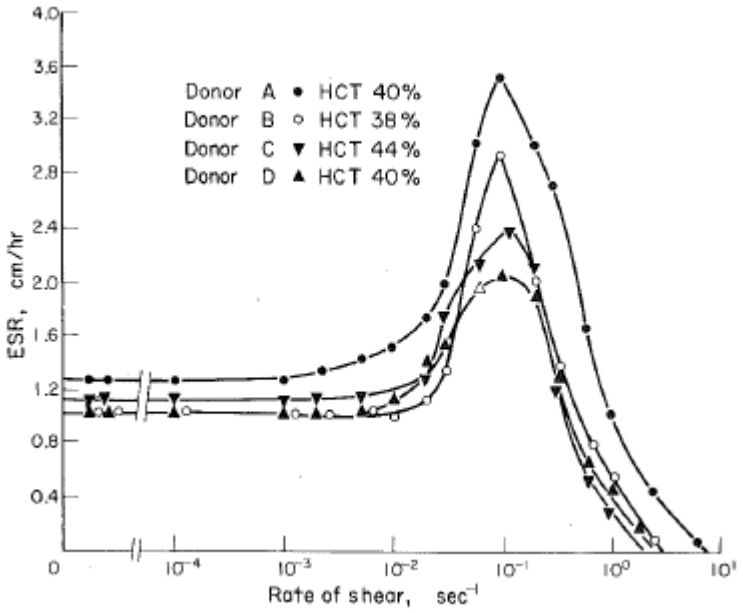

Figure 5-1. From [29]: Plot of experimental data demonstrating the shear dependence of ESR

The shear-ESR relationship illustrated in Figure 5-1 might help to explain the major shortcomings of prior cell transport descriptions: overestimating ESR from RBC bias and misestimating WBC bias from said ESR estimates. The ESR values inferred from RBC bias pertain to a sedimenting shear flow. Thus, if flow conditions are such that ESR-elevating shear rates are present, inferred-ESR values might exceed the published ESR values which pertain to static whole blood transport. With respect to the inability to use inferred-ESR values to predict WBC bias: the difference in flow rate between the RBC and WBC measurements will alter the velocity profile and, in turn, the shear acting upon the flow. Consequently, it would be faulty to apply inferred-ESR values to WBC measurements from the comparison study as the shear-enhanced sedimentation should have affected the two measurements to different extents.

Chapter 6: A Gravity-Bias-Free Transport Domain

A primary motivation of this research is to advance healthcare through the development of technologies which could enhance the scope of tests available at the point of care. The experimental testing of devices in Chapters 3 and 4 demonstrated the profound effects of gravity upon cell transport in creeping whole blood flows. The scope of design considerations were then expanded through discussion of key, secondary phenomena in Chapter 5. In order to satisfy the research objective, these findings should be converted into meaningful device revisions which give rise to a cell-dispensing technology which is unbiased by gravitational effects. In this chapter, an optimized, gravitationally-unbiased transport domain is developed and tested within a device such that performance of this revised device can be compared with that of the initial, gravity-biased device.

6.1 Cell-Dispensing Domain

The optimized transport domain consists of a primary blood-holding volume having an inlet for blood loading and blood propulsion (propulsion is again provided by an external pump which delivers ‘pusher fluid’ at a controlled rate) and an outlet which links the holding volume with an adjoining channel which, in turn, links the cell-dispensing circuit with a cell-processing circuit. As the transport through the domain outlet will define the ‘cell-dispensing’ accuracy of this domain, cell distributions and motion in the ‘transition control volume’ which links the blood-holding domain to post-outlet channels is of key interest. Each of the three key domain elements (blood-holding volume, outlet, and

transition control volume) is illustrated in Figure 6-1 which provides a detailed view of the revised cell-dispensing domain.

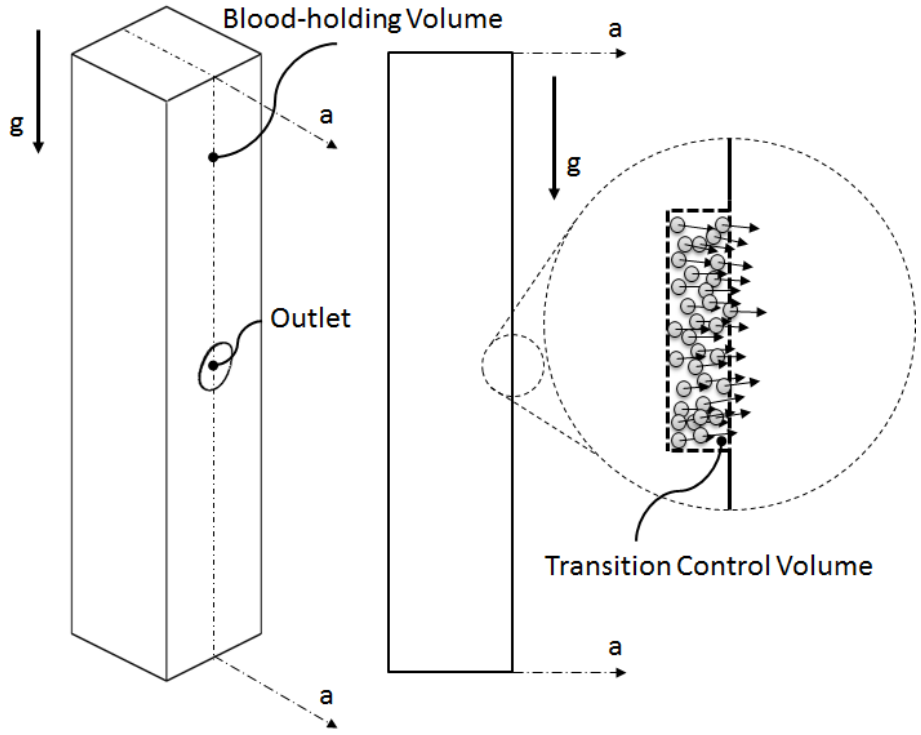

Figure 6-1 Detailed view of blood-holding volume, outlet, and transition control volume

6.1.1 Principles of Operation

The blood-holding element, which acts as a sustained source for gravitationally-unaffected blood, is a straight, vertically-oriented channel having a relatively large (read: non-micro), uniform cross section. Within this element, where the bulk flow velocity will be on the order of an average ESR value (~30 [mm/hr]), cell transport is dominated by sedimentation. As such, this portion of the transport domain will exhibit the

characteristic phase regions found within a sedimenting medium: packing, suspension, and supernatant. For whole blood, these phase regions are packed cells, pristine (whole) blood, and plasma, respectively. The spatial relationship of these phases is shown in Figure 6-2 wherein the composition of the sedimenting domain is shown to be a function of time. At the outset of the sedimentation process, the entire height of the sedimenting body is filled with homogeneously-distributed cells. With time, a cell-free plasma region forms above the cell suspension while a packed-cell region forms below. The interfaces separating these phases are represented by the solid and dashed curvilinear lines, respectively.

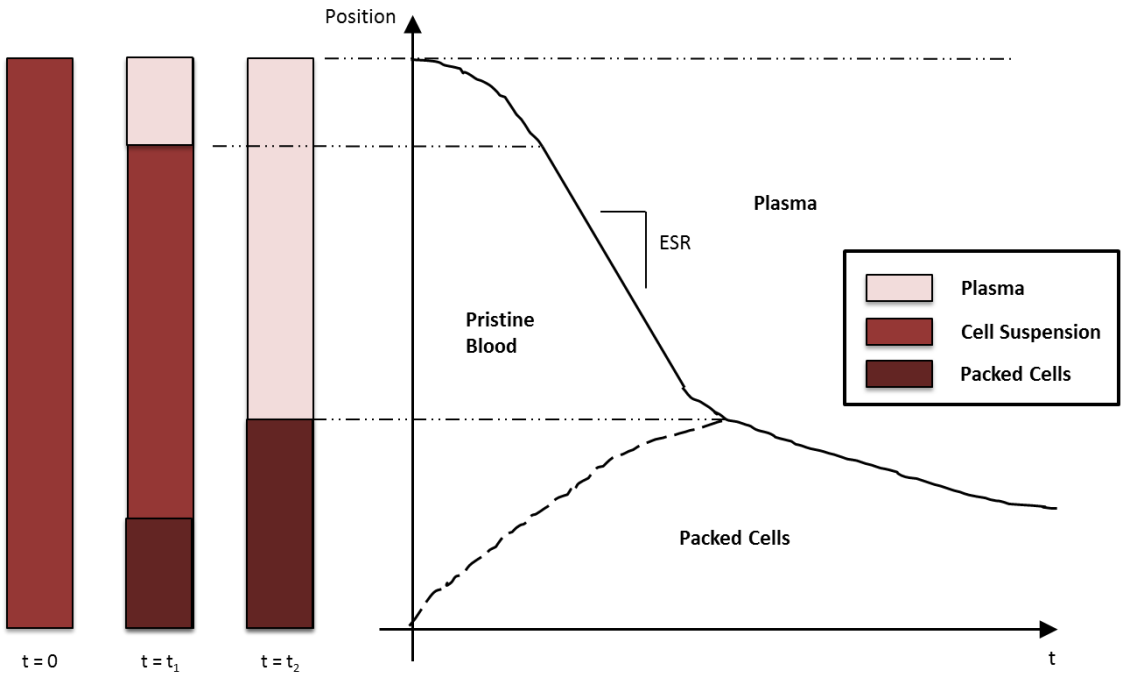

Figure 6-2 Time-lapse diagram of phases within sedimenting whole blood

Before the upper and lower interfaces converge, the sedimenting domain contains a region of whole blood which, although cells are moving in the vertical axis, should have a spatial composition which is reasonably similar to the blood composition at (t=0). This sustained spatial distribution can be leveraged as part of a means to achieve gravitationally-unbiased cell transport.

6.1.2 Circumventing Gravitational Dispensing Bias

Within the sedimenting domain, red and white blood cells are transported in the gravity-parallel direction independently of bulk advection due to the overriding sedimentation process. In order for that gravity-parallel motion to not exaggerate or inhibit transport of cells across the outlet, the normal vector of the sedimenting domain's outlet surface is made to be perpendicular to gravity. Since the outlet's normal vector defines the effective streamwise flow direction of dispensed cells, the vertical-axis motion brought about by gravity does not affect the channel-wise velocity of cells as they exit the blood-holding domain.

The transition control volume dictates the cell dispense rate in that the cells transported across the outlet plane are subsequently transported through the adjoining channel and into the cell-processing portion of the device. Although the exact velocity distribution within this control volume will vary with sample rheology, domain geometry, and bulk flow rate, the rate of cell dispensing $\left(\dot{n}_{dispensed}\right)$ can be controlled with careful management of the bulk volumetric flow rate through the outlet and maintenance of the

spatial distribution of cells adjacent to the outlet. Mathematically, this conjecture is confirmed by the following descriptions of volumetric flow rate and particle transport rate for elements on the outlet surface:

$$d\dot{V} = u_{\hat{n},bulk} * dA, \;\; d\dot{n}_{cells} = \frac{c_{cell} * \; dV \; * \; \bar{u}_{\hat{n},cells}}{ds}$$

$$d\dot{n}_{cells} = \; c_{cell} * \; \bar{u}_{\hat{n},cells} * dA \tag{6-3}$$

If the spatial distribution of cells within the transition control volume is sufficiently representative of the blood sample $\left(c_{cell} = \; c_{reference} \right)$ and the outlet-normal interphase motion is negligible $\left(\bar{u}_{\hat{n},cells} = u_{\hat{n},\; bulk} \right)$ Equation (6-3) can be re-written as Equation (6-4) the surface integral of which reflects a bias-free cell-dispensing operation.

$$d\dot{n}_{dispensed} = \; c_{ref} * \; d\dot{V} \tag{6-4}$$

Here, interphase motion is minimized by maintaining a gravity-perpendicular outlet vector. Meanwhile, reference-unity of the outlet-adjacent cell concentration will be dictated by the transport taking place within the blood-holding volume. The latter consideration, here, is the facet of device operation to which the whole blood phenomena described in Chapter 5 are most pertinent. The following section discusses the way in which both leukocyte margination and shear-enhanced sedimentation factor into the blood-holding domain design.

6.2 Sustaining Cell Concentrations

Transport within the sedimenting domain must be managed in such a way as to ensure that red and white blood cell concentrations within the transition control volume are representative of the whole-blood sample being analyzed, $(c_{cell} = c_{reference})$. To that end, there is a number of design constraints concerning the whole-blood phenomena detailed in Chapter 5:. The following sections provide a context for discussion of concentration 'maintenance' and discuss the particular way in which the effects of each prescribed phenomenon will be minimized.

6.2.1 Problem Formalization

In order for the revised cell-dispensing domain to adhere to Equation (6-4), red and white blood cell concentrations must be uniform and equal to the reference-indicated value within the transition control volume for a duration that is at least equal to that of a sample analysis (~4 minutes). The spatial composition of cells within the transition control volume is the result of transport taking place within the surrounding sedimenting body. The specifics of this transport will depend upon several uncontrollable factors such as sample rheology and sedimentation characteristics, as well as device-design parameters such as the rate of and direction from which bulk flow approaches the blood-holding-volume outlet, and the cross-sectional dimensions of the volume itself. In considering the optimization of the design parameters, there are two key conditions which should be met:

1. The initial distribution of cells within the blood-holding volume must be uniform and equal to the concentration within the un-processed blood specimen
2. The bulk transport of cells within the blood-holding volume must be configured in such a way that does not compromise the initial conditions

6.2.2 Initial Cell Distribution

In 5.1, the scope of considerations regarding device-meaurement bias was extended to include elements of sample analysis which preceded the sedimentation process. This discussion focused primarily on the implications of device loading within the subsequent cell-dispensing process. While the mode of bias prescribed in that section pertained to the impact of sample inhomogeneity upon dispense-phase cell transport, the known causes of sample inhomogeneity discussed there are equally valid in the present context. Specifically leukocyte margination, the shear-induced inhomogeneity of WBCs within a whole blood flow, is a key consideration for the design of the blood-holding volume.

While it would be convenient for the sake of optimization, leukocyte margination is not readily described by mathematical means. In fact, the knowledge base regarding leukocyte margination is limited to experimental characterization of margination within microscale domains wherein passage size, hematocrit and wall shear rate have been shown to have substantial effects upon the cross-sectional distribution of white blood

cells [22] [30]. While these parametric analyses provide insight regarding margination in micro passages, there is limited information regarding WBC distributions in passages larger than 50[μm]. The lack of characterization in larger passages is likely due to the obscuration of in-flow WBCs by the optically-dense RBCs [31].

The lack of a mathematical means for predicting margination poses a substantial hurdle for dispensing-domain optimization. While an absence of theoretical utilities might otherwise be overcome through visual observation of WBC motion, existing literature refutes this as a valid means of development due to the inherent interference of red blood cells. Because red blood cells are the driving force in margination [32], there is no way to remove the visual interference without disrupting the physical system. As such, leukocyte margination, the key concern with regard to initial cell distribution within the blood-holding volume, is not a directly verifiable design consideration. In light of this fact, an appropriate design direction must be selected to minimize margination effects. In turn, the bias of WBC dispensing will serve to validate the efficacy of the resulting design in minimizing margination. To that end, it may be possible to minimize the extent of WBC inhomogeneity through diligent selection of the blood-holding volume's dimensions.

The blood-holding volume has three primary dimensions. The first is the volume's length which must be suitably long as to afford an outlet location which is adjacent to the

cell suspension for the duration of an analysis. In anticipating a maximum ESR value of 150 [mm/hr], a four minute analyses would result in a 10[mm] advancement of the cell-plasma interface. To provide sufficient separation of the outlet from the top surface of the blood-holding volume, the volume length (l_{bhv}) should be made ~20[mm] long with a centered or below-center outlet location. The blood-holding volume has a rectangular cross-sectional profile; the height (h_{bhv}) and width (w_{bhv}) of which round out description of the blood-holding volume's geometry. The height and width of the cross section can be held equal; the smallest dimension will be largely defining of shear effects so there is not much utility in varying the two independently.

6.2.2.1 Margination Development as a Function of Channel-wise Position

Leukocyte margination refers to the shear-induced redistribution of white blood cells within the profile of a whole blood flow. For a given geometry, sample rheology, and bulk flow rate, white blood cells will be distributed at characteristic locations within the flow. An example distribution, from [22], is shown in Figure 6-3 wherein white blood cells are shown to be substantially more concentrated near the channel edge and less concentrated near the channel center. The illustrated cell distribution was observed at the outlet of a 3.6[mm] long, 69 [μm] diameter tube. The extreme length of the tube relative to its diameter ensures development of the cell distribution. This notion--that of a margination-development length—presents a route by which margination effects can be minimized.

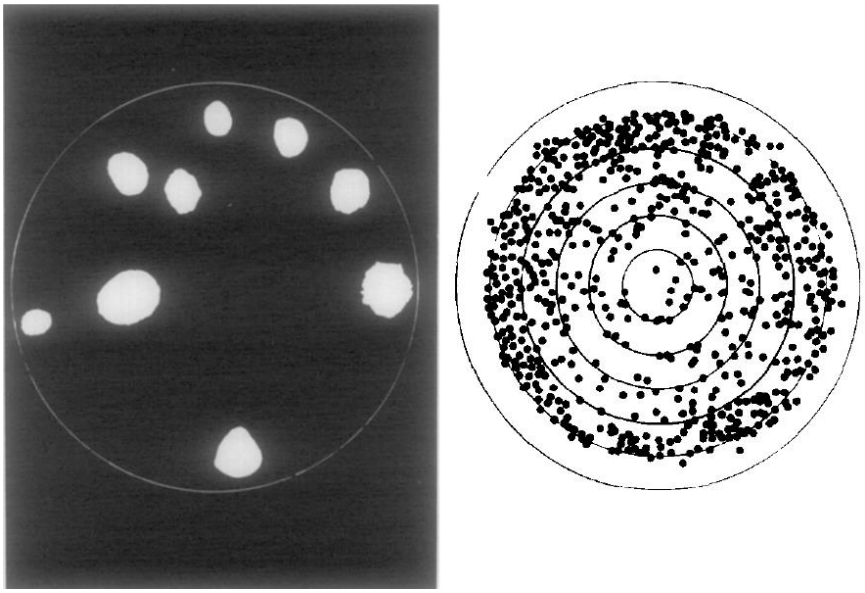

Figure 6-3 From [22]: Left panel: Photograph (multiple exposure) of the distal opening of a 69- μm tube with fluorescent leukocytes passing the focal plane of the objective. Right panel: Division of the tube cross section into six concentric rings of 5.8- μm width. The black dots represent the position of WBCs passing the focal place of the microscope.

While margination is an innate consequence of shearing whole blood, the extent of margination can be managed by configuring the flow domain such that the characteristic length over which margination develops is significantly greater than the pertinent length over which blood is sheared in practice. In other words, the cross section of the blood-holding volume can be designed such that shear through the blood-holding volume's length produces an insignificant change in WBC distribution. Intuitively, it can be assumed that the length required for margination to have a profound effect on white blood cell distribution $\left(l_{margination}\right)$ will increase with the characteristic length scale of

the domain (w_{bhv}). Additionally, it is desired that the domain length (l_{bhv}) be less than the characteristic length of margination as expressed in Equation (6-5).

$$l_{bhv} / l_{margination} < 1 \tag{6-5}$$

If the characteristic margination length does in fact increase as the passage size increases, the ratio of domain length (l_{bhv}) to margination length ($l_{margination}$) can be minimized by expanding the blood-holding volume cross section. While this assertion rests on a number of intuitive assumptions, the lack of theoretical and experimental means for verifying a given design results in the need for guess-and-check; the only way to verify that a particular domain prevents significant margination is infer the presence or absence of margination from adherence of observed cell transport rates to the prescribed process description.

6.2.3 Bulk Cell Transport

In addition to determining the extent of WBC margination, the blood-holding-volume cross section is a significant factor in the bulk transport taking place therein. To explain, a diagram of transport near the blood-holding volume outlet is provided in Figure 6-4. There, the bulk volumetric flow rates into the outlet region is said to be equal to the volumetric flow rate through the outlet. Additionally, the cumulative cell transport into the outlet-adjacent region of the volume is equal to the sum of the outlet transport rate and rate of change in the number of bounded particles.

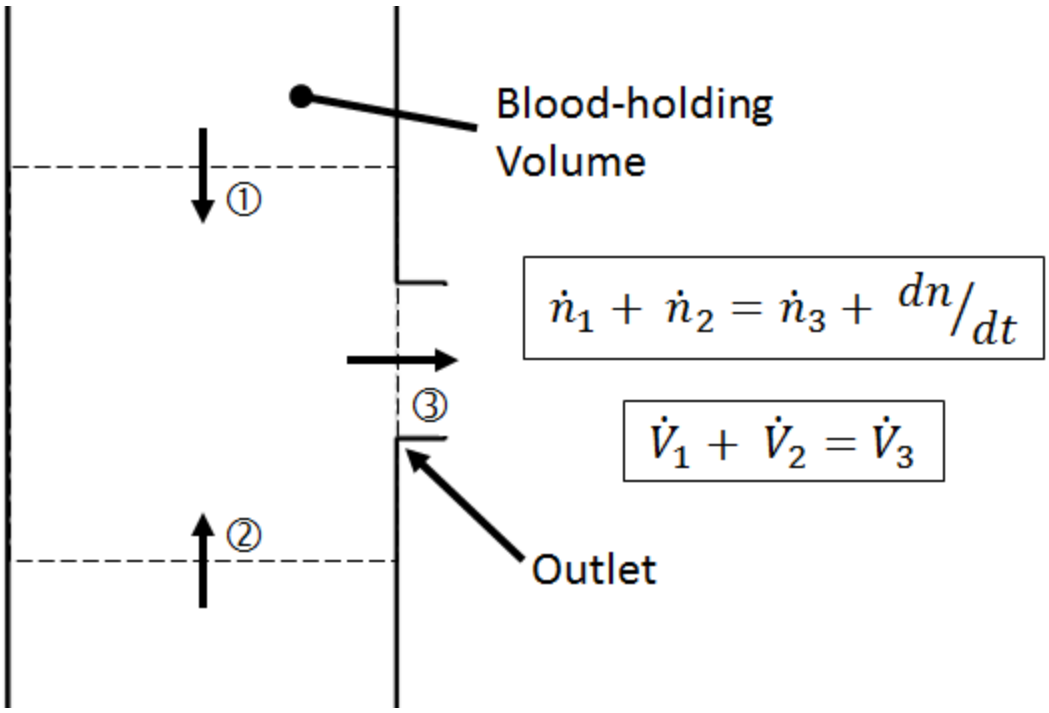

Figure 6-4 Transport diagram for the central region of the blood-holding volume

In practice, $(\dot{V}_{pusher\ fluid} = \dot{V}_1 + \dot{V}_2)$ while the ratio of $(\dot{V}_1)$ to $(\dot{V}_2)$ depends on the manner of pusher fluid delivery into blood-holding volume. For each of the devices utilized henceforth, the relative buoyancy of the pusher fluid (DI water) requires that $(\dot{V}_2 = 0)$ so as to avoid dilution of the blood sample; fluid injected at the bottom of the blood-holding volume would float up and into the cell suspension. As such, for the devices tested within this research: $(\dot{V}_1 = \dot{V}_{pusher\ fluid})$. The asymmetry of the bulk flow within the system is cause for concern.

The desired operation of the revised dispensing geometry assumes that the sedimentation effect upon cell transport will be inversely proportional in the upper and lower portions of

the blood-holding volume; gravitationally-enhanced transport of red cells from the upper half of the volume ($\dot{n}_1$) is balanced by the gravitationally-inhibited RBC transport coming from the lower half. Thus, the absence of bulk flow in the lower portion of the blood-holding volume requires that the bulk flow in the upper portion of the domain not affect the sedimentation process. The shear enhancement of sedimentation described in Section 5.2 is especially relevant with regard to this necessary condition. Specifically, it is important that the blood-holding volume cross section and the bulk volumetric flow rate **do not** produce fluidic shear rates in the sedimentation-enhancing range.

6.3 Experimental Testing of the Revised Dispensing Domain

While the principles behind the optimized transport domain promise that it may be a sound method for reducing gravitational transport bias, experimental testing is the true measure of an analytical device. As such, it is necessary to implement the optimized transport domain within a microdevice as a means for gauging the efficacy of the optimized cell-dispensing circuit. In order to demonstrate the change in device performance brought about by the transport-domain optimization, a new microdevice design was tested using the same comparability-test format that had yielded observations of gravity-enhanced transport. The following sections describe this new microdevice, its features, the measurement protocol that is executed within the device, and the experimental test procedure used to gauge the revised device's performance.

6.3.1 Microdevice

An overview of the optimized microdevice, containing the reconfigured cell-dispensing feature, is shown in Figure 6-5. As with the prior microdevice, the revised device's fluidic circuit takes a three-part format beginning with cell dispensing, dispensed cells then enter a cell-processing circuit, and the processed cells eventually enter a cell-focusing feature where they are analyzed. While the cell-focusing portion of the revised device does not differ in format from the previous device, both the cell-dispensing and cell-processing features were modified. As such, subsequent sections provide detailed information regarding the structure and functionality of these device features.

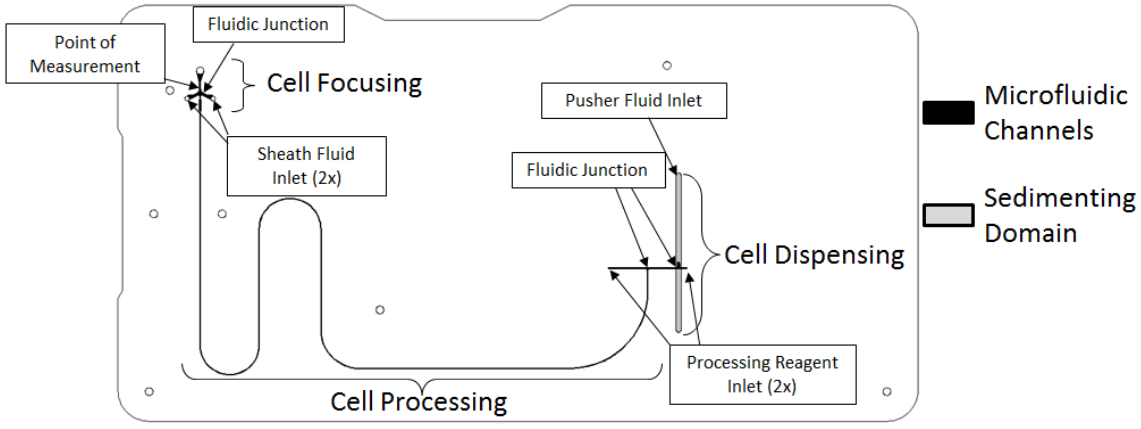

Figure 6-5 Annotated layout of the optimized microfluidic device

6.3.1.1 Cell Dispensing

The revised microdevice makes use of an embodiment of the gravity-unbiased cell-dispensing domain. As described previously, this domain has undefined dimensional parameters and post-outlet geometry. Intuitively, the sedimentation domain must have a

length which allows for an outlet position which falls between the phase interfaces of the sedimenting whole blood. Because of this, the domain is 20 millimeters long; long enough that a sample with an ESR of 150 [mm/hr] will not result in the cell-plasma interface eclipsing a centrally-located outlet during a test that is four minutes in duration.

The sedimenting domain's cross section is most easily fabricated as a rectangular channel. Additionally, as the smallest cross-sectional dimension is likely to instigate shear-dependent physics such as margination (shear-induced inhomogeneity of WBCs within the flow profile), and because minimization of specimen volume is always beneficial in point-of-care devices, it is sensible to utilize a unity aspect ratio in constructing the sedimenting domain. Thus, the sedimenting domain within the optimized microdevice has a square cross-sectional profile. The choice of the appropriate dimension for the domain cross section is a complex question. On the one hand, a large cross section further minimizes the shear-induced transport effects (such as margination and sediment enhancement). Oppositely, reduction of the cross-sectional area of the sedimenting domain will decrease the effect that sedimentation imbalance between the upper and lower domain halves would have upon the outlet-adjacent domain region. Here, the chief cause of sedimentation balance is itself a shear-induced sedimentation enhancement (overview provided in Section 5.2). Because shear-enhanced sedimentation can be substantially minimized with an increase in cross-sectional area and subsequent reduction of shear, the desired cell-dispense accuracy was achieved through the selection

of a cross-sectional area which minimizes the WBC-biasing effects of leukocyte margination and ensures that the in-domain shear levels are such that ESR enhancement due to fluid shear is does not occur: the cross section of the cell-dispensing volume is a 0.8x0.8 [mm] square.

6.3.1.2 Cell Processing

Within the scope of cell processing, there are a number of key functions which must be provided in order to convert whole blood into singular, analyzable cells. Specifically, aggregates of cells within whole blood must be broken up so that the individual cells are exposed to cell-preparation reactants for a sufficient duration to bring the particular reaction to completion. In a macro-scale system, these actions may be as simple as to inject a volume of blood into a large volume of processing reactant and vigorously stirring the mixture for an appropriate duration. On the micro scale, mixing of particulates such as blood cells with liquid chemicals is complicated by the fact that momentum-dependent mixing is limited or altogether absent. As a consequence, penetration of processing chemicals into the whole blood matrix is almost entirely dependent upon diffusion. Therefore, a device is well served by a reduction in the path length of diffusion which must be penetrated as a precursory step to cell-chemical reaction.

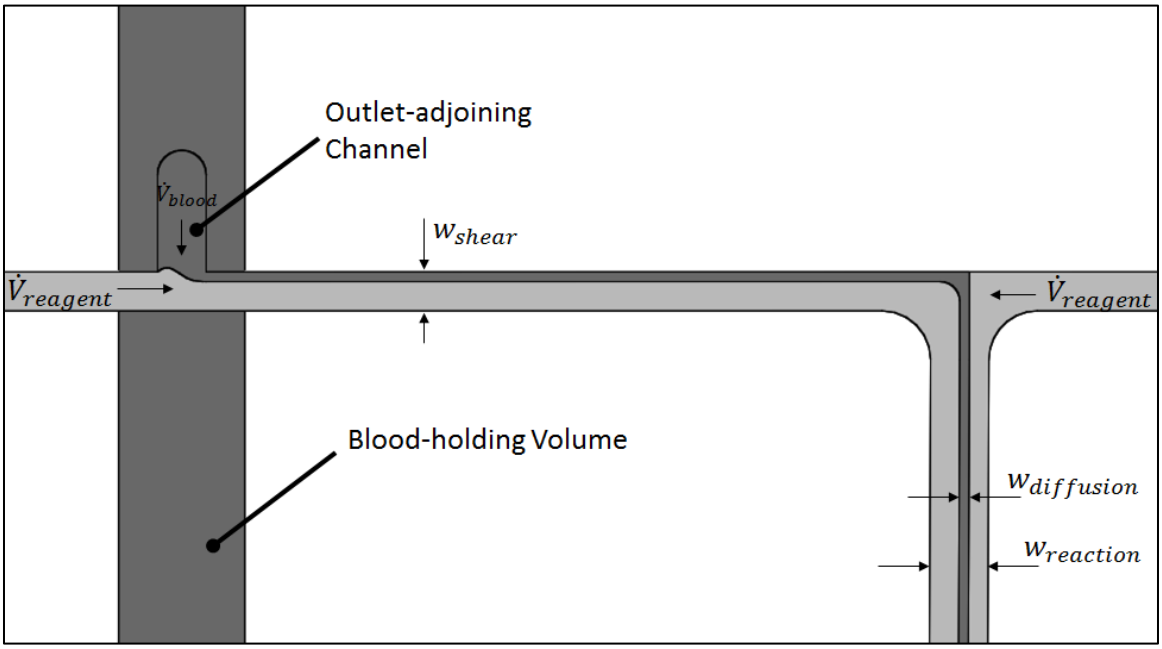

Figure 6-6 Illustration of the initial portion of the optimized cell-processing circuit

In the cell-processing circuit shown in Figure 6-6, whole blood combines with a processing reagent stream at a T-junction. The reactant crossflow traps blood against the inside wall of the outlet channel where cells and cell aggregates are sheared. The shear along this wall is configured to disaggregate whole blood, resulting in a downstream flow of individualized cells. Downstream of the blood-reagent junction, there is a second T-junction. At this T-junction, the cell-reactant combined flow (an ordered side-by-side flow, not a mixture) meets with a second reactant flow. As the cell-reagent flow exits the second T-junction, the disaggregated blood cells are entrained by the reagent flows. In the revised device, the width of the cell-containing portion of the exiting flow, which can be described by a Hele-Shaw model, is configured to be near to or less than the size of a

blood cell. As such, the time of diffusion within the revised device is negligible compared to the time of reaction.

With the time of diffusion approaching zero, the residence time of cells within the processing reactant needs to be configured to match the cell-reactant reaction time, a reasonably constant factor. An optimal residence time was determined to be (~10[s]) and was implemented by adjusting the volume of the lengthy channel downstream of the cell-processing junction such that the quotient of that channel volume over the volumetric flow rate of the side-by-side-by-side flow was equal to the estimated reaction time.

6.3.2 Measurement Routine

For the previous experiments, the overwhelming abundance of red blood cells within whole blood required that a supplementary fluid step be used to perform red blood cell quantitation. For the current set of experiments, an upgraded electronics system enables the elimination of the supplementary fluidic step. As such, both the RBC and WBC-concentration measurement routines consist of the establishment of a steady transport state for which the cell transport rate at the point of detection are assumed to be consistent with Equation (1-1). The fluidic pumping rates and process timing for testing of the revised microdevice are detailed in routine 6A, provided in Appendix B.

6.3.3 Experimental Procedure

In order to gauge the efficacy of the gravitationally-unbiased transport domain, the revised microdevice design was tested using a comparison study similar to that used to analyze the predicate device in Chapter 3. For this comparison study, 20 unique blood specimens were analyzed. Each analysis yielded a value for both white and red blood cell concentration. Because the cell-dispensing process is time-invariant for the revised device, there is no need to exclude one or the other measurement based on the need for development of a steady sedimentation condition. Therefore, each analysis provided a pertinent indication of both RBC and WBC measurement bias for the gravity-negating domain. Each analysis was performed using a constant measurement routine: routine 6A.

6.4 Results

6.4.1 RBC Concentration Measurements

The RBC concentration of each sample was measured using both the optimized microdevice and a reference instrument: an Abbott Cell Dyn 3200. As in the previous comparability study, the reference instrument provided the standard against which the accuracy of revised device measurements can be gauged. A datum for each measurement is provided in Figure 6-7 which illustrates the correlation between RBC measurements made on the microdevice and reference instrument. Overall, the data demonstrates that the revised device produced a weaker correlation ($R^2 = 0.74$ vs $R^2 = 0.85$) but was closer

to unity with the reference instrument (slope = 0.90 vs slope = 0.65) than the initial microdevice.

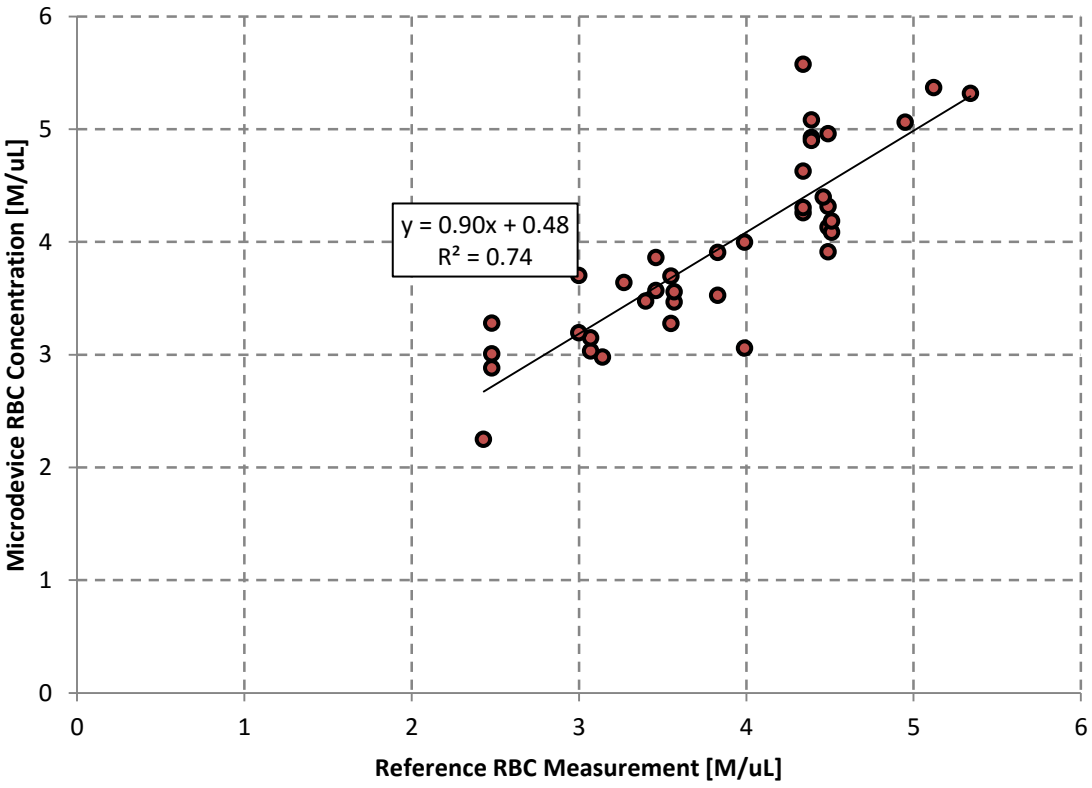

Figure 6-7 Scatterplot illustrating the correlation between microdevice and reference instrument measurements for RBC concentration

6.4.2 WBC Concentration Measurements

A correlation of the measurements generated by the microdevice and reference instrument is provided in Figure 6-8. The plot of WBC measurements show a stronger correlation (R^2 = 0.96 vs R^2 = 0.91) and closer unity to the reference instrument (slope = 0.96 vs slope = 0.62) than the initial microdevice.

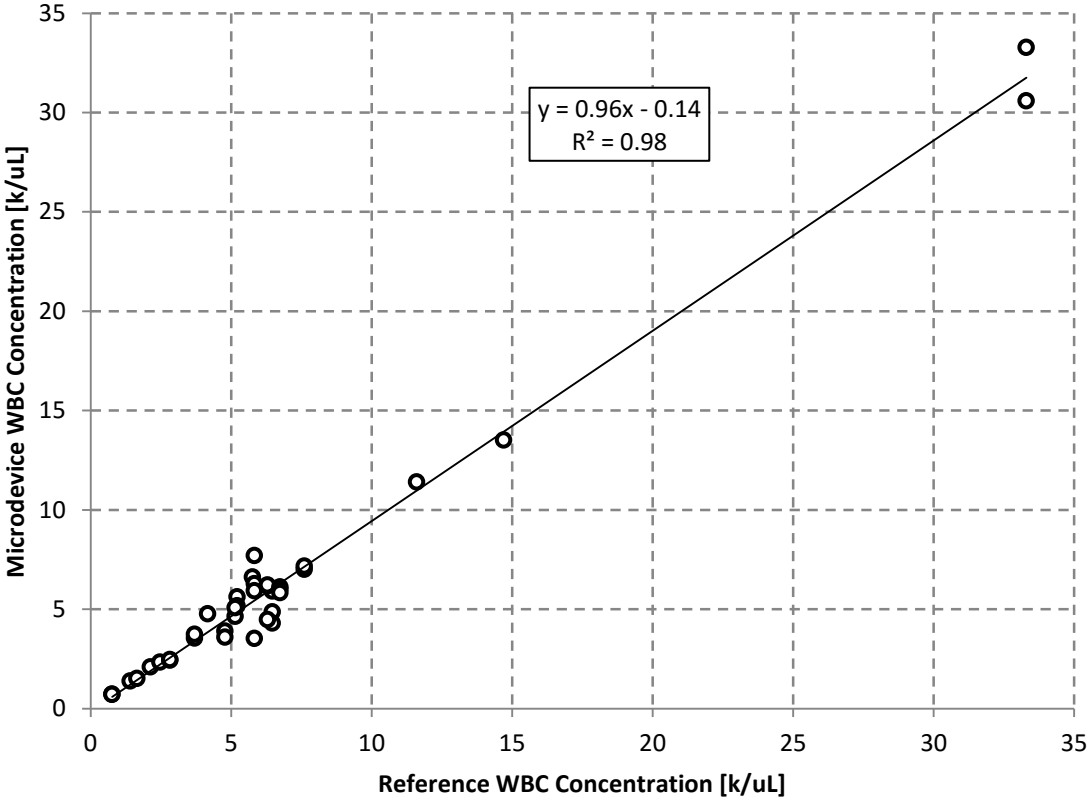

Figure 6-8 Scatterplot illustrating the correlation between microdevice and reference measurements of WBC concentration

6.5 Conclusions

A primary purpose of optimizing the cell transport domain was to circumvent the RBC-transport enhancement and WBC-transport inhibition which gravity had instigated in the initial microdevice. To that end, the revised transport domain appears to have been somewhat effective. The extent of RBC and WBC bias in the low-RBC range, as plotted in Figure 6-9, appears to be less dramatic than was the case for measurements taken on the initial microdevice.

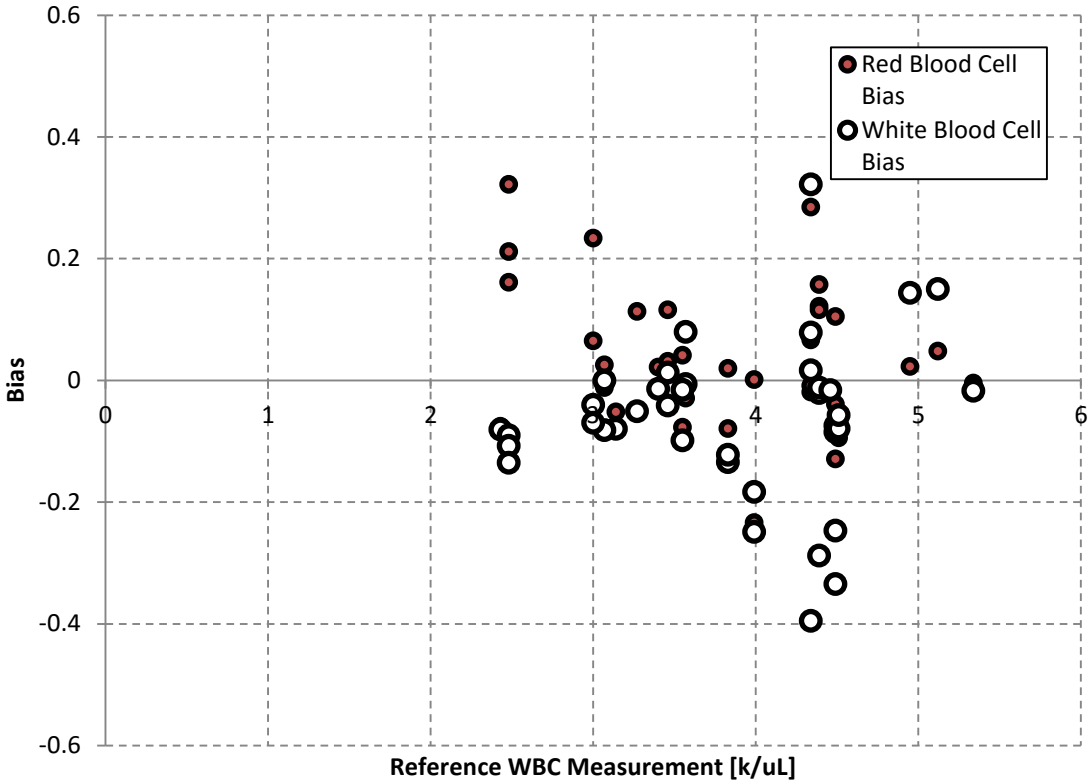

Figure 6-9 RBC and WBC biases for Concentration Measurements using the Optimized Microdevice

Still, it seems that the rate of cell dispensing facilitated by the revised cell-dispensing domain does not fit description by Equation (1-1). In fact, over the tested RBC range, RBC and WBC bias again show a general trend of inverse proportionality. While this trend is akin to that observed in bias plots of initial device measurements, the mechanism by which the trend in Figure 6-9 was found to develop is indirectly related to the principles of operation stated for the revised cell-dispensing domain. An explanation of the biasing mechanism and testing of a new device based on the unforeseen facet of cell transport is provided in Chapter 7:.

Chapter 7: Directionality of Outlet Transport

In Chapter 6:, principles were set forth which described the manner in which a gravitationally-unbiased, cell-dispensing domain would produce RBC and WBC concentration measurements which were more accurate than measurements generated by the gravitationally-biased transport system tested in Chapter 3:. While measurements facilitated by the revised transport domain (that tested in Chapter 6) were reasonably more 'true' to measurements generated on a reference instrument, the change in performance relative to the initial device was insignificant. For each of the previously-tested devices, RBC and WBC measurement bias tended to be inversely proportional with device-generated RBC measurements exceeding reference values and WBC measurements coming short of reference values by a similar magnitude.

For the initial microdevice, the inverse bias of cell-concentration measurements was linked to the whole blood sedimentation process by which red blood cell transport was enhanced by gravity and, conversely, white blood cells transport was inhibited. Naturally, this experience provided a natural path of inquiry for the mechanism by which inverse measurement bias was generated by the revised transport system. However, the principles by which the revised cell-dispensing domain was derived were specifically aimed at negating gravitational effects. By what means, then, would sedimentation factor into cell transport? Although the foundation of domain operation set in Chapter 6: is

sound, the stated conditions omit a simple practical consideration: The formula for outlet cell transport prescribed in Equation (6-4), while valid within the sedimenting domain, is invalid in the horizontal, outlet-adjoining channel wherein sedimentation produces phase separation. The phase separation in the outlet-adjoining channel violates the assumptions on which Equation (6-4) is founded. Reverse flow across the outlet plane represents a deviation from the ideal conditions which can give rise to biased transport. The following sections further this notion, describe the physical cause of reversed outlet flow within the prior microdevice, detail a simulation of the mechanics of said cause as well as a mitigating design change, and outline the experimental testing of a microdevice which makes use of the gravity-bias-negating domain and revised outlet-adjoining channel.

7.1 Outlet Flow Recirculation as Transport Bias

To expand upon the prior notion—that reversed flow across the dispense-domain outlet results in an effective transport bias—consider the transport relationship for the example velocity profiles in Figure 7-1. There, profile (a) represents an outlet velocity condition which includes a flow recirculation while profile (b) represents an outlet velocity condition that is free of recirculation. Within the context of this discussion, the profiles represent hypothetical, outlet-normal velocity profiles at the blood-holding-volume outlet.

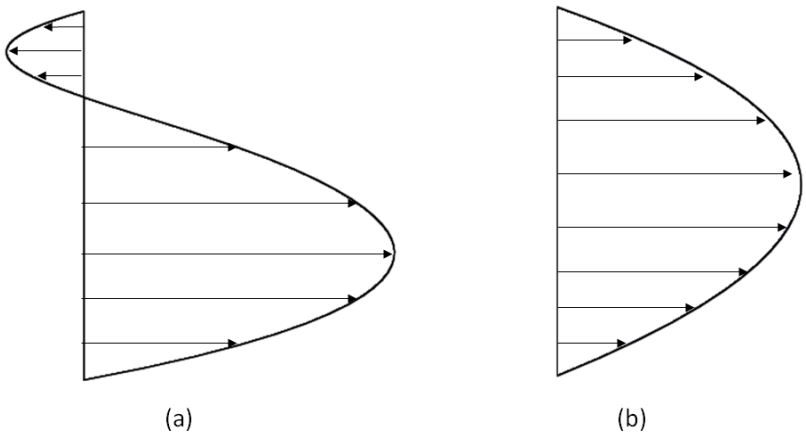

Figure 7-1 Model velocity profiles for reversed (a) and forward (b) bulk transport

Per the discussion of volumetric transport in Chapter 6:, the surface integral of each profile must be equal to the pusher fluid flow rate $\left(\dot{V}_{pusher\ fluid}\right)$. This implies that, for profile (a), the forward bulk transport must be equal to the pusher fluid flow rate **plus** the reversed volumetric flow rate: expressed in Equation (7-1).

$$\dot{V}_{forward,(a)} = \dot{V}_{pusher\ fluid} + \dot{V}_{reverse,(a)} \quad (7\text{-}1)$$

With that, the cell transport in the forward-moving portion of profile (a) can be described as in Equation (7-2) wherein the concentration of forward-moving cells is determined by the blood-holding volume and is therefore believed to be equal to a reference-indicated concentration.

$$\dot{n}_{forward,(a)} = c_{ref} * \left(\dot{V}_{pusher\ fluid} + \dot{V}_{reverse,(a)}\right) \quad (7\text{-}2)$$

Cell transport within the reverse-flow portion of profile (a) complicated by the unknown cell distribution downstream of the blood-holding-volume outlet (recall the context of this discussion). Here, it is sufficient to apply a transport-averaged $\left(c' = \frac{\dot{n}}{\dot{V}}\right)$, effective cell concentration that satisfies the identity given in Equation (7-3).

$$\dot{n}_{reverse,(a)} = c' * \dot{V}_{reverse,(a)} \quad (7\text{-}3)$$

Ultimately, the flow reversal will result in a net cell transport equivalent to that described in Equation (7-4).

$$\dot{n}_{(a)} = c_{ref} * \left(\dot{V}_{pusher\ fluid} + \dot{V}_{reverse,(a)}\right) - c' * \dot{V}_{reverse,(a)} \quad (7\text{-}4)$$

As previously stated, Equation (7-4) confirms that for a reverse flow in which reversing cell concentrations do not match the reference-indicated concentration, the gravity-negating transport domain will produce transport (and therefore concentration measurements) which deviate from expected. The extent to which a given measurement will deviate from expected is dependent upon the concentration of a given cell type within the flow recirculation.

7.2 Density-Driven Outlet Flow Recirculation

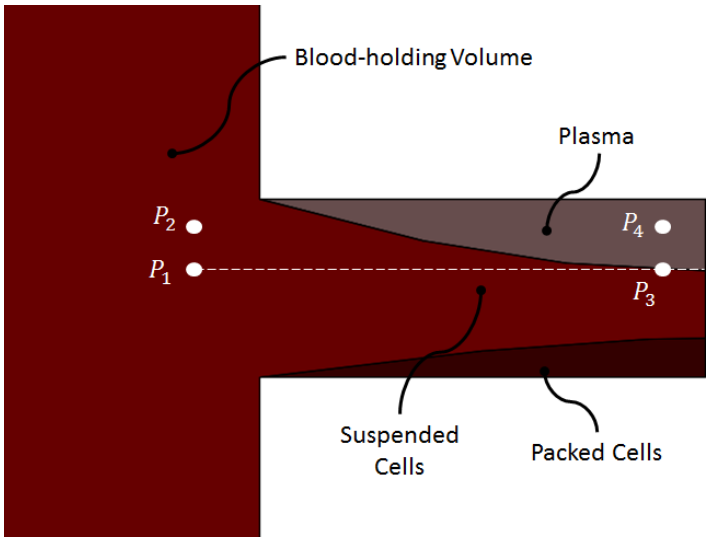

Figure 7-2 Illustration of phase separation in outlet-adjoining channel

Figure 7-2 illustrates a three-region media separation within the outlet-adjoining channel with cell-free plasma along the upper channel surface, below which is a region of suspended cells and below which is a packed-cell region. While the indicated phase boundaries are not physically accurate, they allow the physical concern with phase separation to be illustrated. The bulk flow within the sedimenting domain and adjoining channel is extremely slow. As such, the dynamics of cell transport within these volumes should be akin to the transport in a static situation. If, for the sake of argument, the volume shown in Figure 7-2 were left to sit for an extended period under a zero-flow condition, the region of plasma which formed at the top surface of the horizontal channel

would be propelled backward into the suspension-filled sedimentation domain. The jettison of plasma from the horizontal channel is due to the pressure difference brought about by phase separation. To explain this, four points of pressure reference are provided in Figure 7-2. Because the theorized system is at rest, P_1 and P_3 can be assumed equal since they are at equal height and the isobaric line connecting the two points falls within a constant phase. P_2 relates to P_1 through Equation (7-5) from hydrostatics: P_2 is less than P_1 by an amount equal to the specific weight of the cell suspension multiplied by the distance separating the two points.

$$P_2 = P_1 - \gamma_{suspension} * (y_2 - y_1) \tag{7-5}$$

Likewise, P_4 and P_3 are related by Equation (7-6) which is identical in form to Equation (7-5) but differs in that the specific weight reflects the plasma phase which separates the two points.

$$P_4 = P_3 - \gamma_{plasma} * (y_2 - y_1) \tag{7-6}$$

Because the specific weight of plasma is less than that of the cell suspension, P_4 differs from P_1 and P_3 to lesser extent than does P_2. Since P_4 and P_2 are at equal height within the domain, the pressure difference between the two creates an unbalanced thermodynamic state which should bring about counter-gradient bulk motion and subsequent viscous stresses which will bring thermodynamic balance to the system. Although this description can be cleanly applied to a static system, bulk flow introduces a great deal of

complexity with regard to the balance between the shearing effect of bulk motion and the phase-separation-based pressure differential. Under rapid flow conditions, it would be expected that viscous effects would drag the plasma phase along the channel regardless of the minute amount to which it was inclined to flow in the channel-reverse direction. Unfortunately, the drastically slow flow rate utilized in the cell-dispensing process does not allow for this physical effect to be ignored. Due to the complexity of the physical system, numerical simulation is an appropriate means for determining the extent to which post-outlet sedimentation will affect outlet transport directionality. The following section details a numerical scheme by which the dynamics within the cell-dispensing domain can be described and provides evidence that the previous microdevice was prone to density-driven recirculation.

7.3 Numerical Simulation of Outlet-adjacent Transport

In order to analyze the outlet-adjacent domain, a Mixture Model of multiphase flow was employed. The Mixture Model is preferred here because the mixture model description contains only one momentum-conservation equation [33]. Thus, there is no need to separate viscous stresses between individual phases. As such, the rheological information provided by the literature can be easily implemented within the model. Similarly, the Mixture Model makes use of an interphase-velocity equation which enables direct control over localized sedimentation rates based on established ESR factors such as hematocrit. The conservation equations within the model ensure that the effects of this

interphase motion are reflected in the mechanics of the transport domain. This is precisely what is desired of the present problem; to determine the effects of a known sedimentation rate upon the transport of whole blood across the sedimenting domain outlet.

The output of the simulation process should be twofold. The first objective is to establish the existence of a density-based flow reversal within the previously-tested cell-dispensing domain. Second, the insight provided by analysis of the previous design should inform domain optimization. The latter of these interests is progressive and will require synthesis of new domain architectures which can be analyzed by the numerical model and, subsequently, tested experimentally.

7.3.1 Mixture Model

The Mixture Model consists of three primary equations. The first, shown in Equation (7-7) is the continuity equation which expresses mixture-mass conservation wherein the mixture is a combination of ‘n’ number of phases. The second equation is the mixture momentum equation. This momentum equation accounts for all energy transfer within the model and, as such deals with tensor quantities of the ‘mixture’ rather than its constituent elements. The momentum equation is stated here as in Equation (7-8). Finally, the mixture model incorporates ‘n’ number of phase-continuity equations: Equation (7-9).

$$\frac{\partial \rho_m}{\partial t} = \nabla \cdot (\rho_m u_m) = 0 \tag{7-7}$$

$$\frac{\partial}{\partial t}\rho_m u_m + \nabla \cdot (\rho_m u_m u_m) = -\nabla p_m - \nabla \cdot \left[\rho_m c_p (1 - c_p) u_{Cp0} u_{Cp0}\right] + \nabla \cdot \tau_m + \rho_m g \tag{7-8}$$

$$\frac{\partial \alpha_p}{\partial t} + \nabla \cdot \left(\alpha_p u_m - D_{Mp} \nabla \alpha_p\right) = -\nabla \cdot \left[\alpha_p \left(1 - c_p\right) u_{cp0}\right] \tag{7-9}$$

Implementation of the Mixture Model requires a number of parameters such as phase densities (here, red blood cells and plasma) which are readily obtained from physiology literature. In addition, models are needed for the viscous effects (τ_m) and interphase velocity$\left(u_{cp0}\right)$.

7.3.2 Relative Velocity

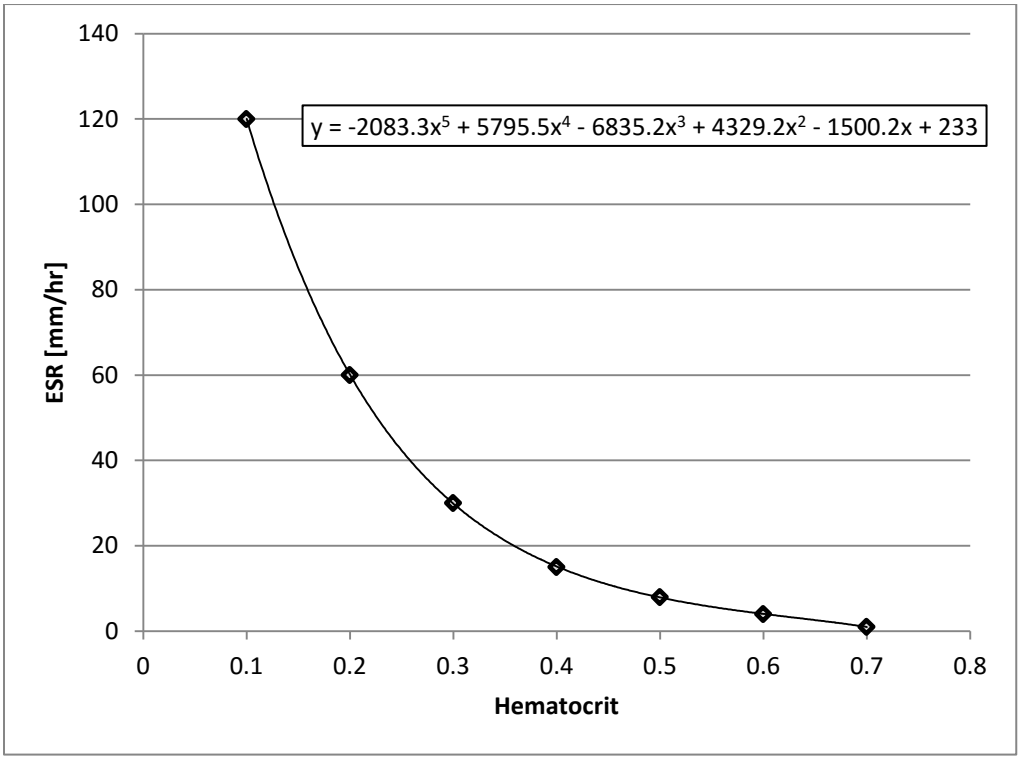

Figure 7-3 Chart of ESR-HCT relationship used within the numerical simulation

The primary form of interphase motion within the target system is gravity-driven sedimentation. Although sedimentation is the product of a phase-density imbalance with the rate being governed by the effective porosity of the suspended phase, the modeling of relative velocity does not need to incorporate the mechanics of this process. In fact, for the system of whole blood described here, it is convenient to apply a description of relative velocity which is a function of its primary intensive determinate: hematocrit (HCT). Borrowing from the data generated in a survey study by Lawrence and Fabry [21], a general function describing ESR as a function of hematocrit was derived. The

data (which were manually selected to coincide with the data bounds from [21]) driving this function, as well as the function itself, are shown in Figure 7-3.

Within the model employed here, the settling velocity of the dispersed (red blood cell) phase is calculated for individual (numerical) cells based on the HCT value of said cell. This scheme effectively captures the appropriate localized sedimentation without the need for computing phase interaction (which is primarily dictated by HCT).

7.3.3 Simulation Strategy

For each of the simulations described here, results were generated by a transient simulation of the cell transport taking place within the fluid domain. Initial conditions for pressure, velocity, and phase volume fractions were generated by a preceding steady-state simulation of each domain. In each of these steady-state simulations, the domain and boundary conditions were the same as in the corresponding transient simulation. However, the interphase velocity was omitted from each of the steady solutions. As a result, the initial solutions provided by the steady-state simulations provided an approximate velocity and pressure field solution for the subsequent transient analysis; the initial phase-volume-fraction field was also specified by the inlet phase volume fraction used in the steady analyses. The conditions for each transient analysis, then, differed from the preceding steady-state simulation only through the incorporation of the previously prescribed relative-velocity model.

7.4 Baseline Domain Simulation

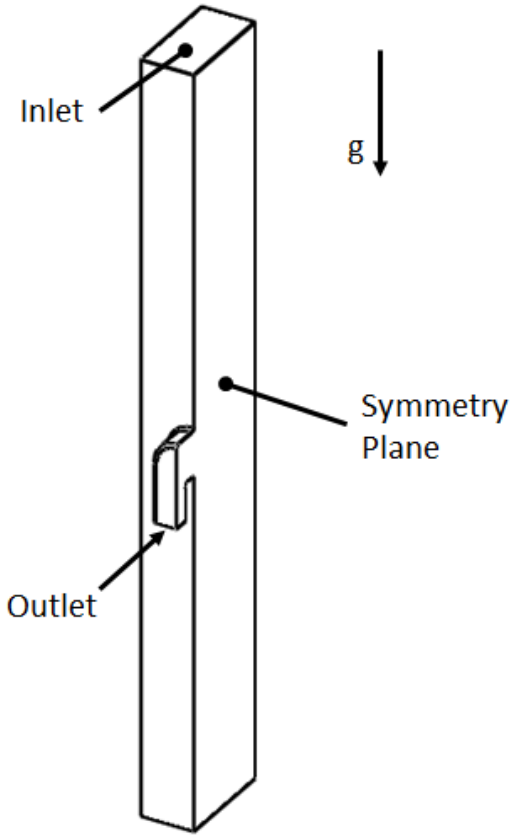

Figure 7-4 Diagram of the baseline simulation domain

The baseline simulation domain, shown in Figure 7-4, consists of a clipped segment of the blood-holding volume which includes the outlet and outlet-adjoining channel. Conveniently, the region of interest allows for further reduction in domain volume by way of planar symmetry: The symmetry plane is indicated in Figure 7-4.

7.4.1 Parameters

Table 3 Baseline domain simulation: material and boundary parameters

Parameter	Value	Units
Inlet Volumetric Flow Rate	0.1	[μL/min]
Plasma Density	1025	[kg/m3]
Red Blood Cell Density	1125	[kg/m3]
Hematocrit (HCT)	0.3	-
Plasma Viscosity	0.0015	[Pa*s]

7.4.2 Results

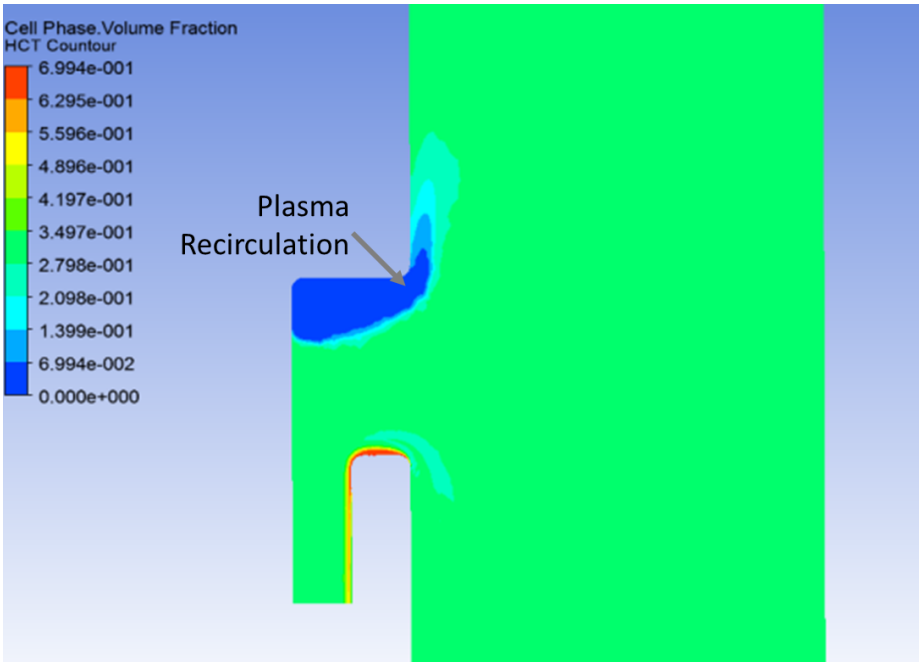

Figure 7-5 Plot of cell-volume fraction within the outlet region of the baseline simulation domain

Figure 7-5 provides a plot of the cell-volume fraction along the symmetry plane of the transport domain for time point (t=10[s]). As indicated in the figure, a pocket of plasma in the upper portion of the outlet-adjoining channel has spurred reverse flow across the

outlet. More surprising than the recirculation is the size of the plasma region itself. It appears that plasma buoyancy is not effectively countered by viscous effects acting to pull the plasma along with the rest of the bulk flow.

This presents an interesting thought: the buoyant stresses propelling plasma toward the upper bound of this channel are, here, countered by viscous stresses that are predominately the product of plasma viscosity. Plasma viscosity is orders less than the viscosity of the plasma-cell mixture. Therefore, if the physical situation were reversed plasma would be buoyantly driven up and out of an upturned outlet-adjoining channel. Meanwhile, packed-cells would form a region similar that of the plasma within the current system. Unlike the plasma, though, packed-cells would have an even higher effective viscosity than the root cells suspension. As such the packed cells, though also compelled toward the main portion of the domain by a density differential, would be more-strongly bound to the bulk flow by viscous stress. Consequently, a 180° turn of the outlet-adjoining channel would result in a trade-off: plasma, the likeliest phase to reverse flow, would be naturally compelled out of the domain while packed cells would be swept along with the bulk flow due to relatively large viscous stresses afforded by cell-containing regions of transport.

7.5 Revised Domain Simulation

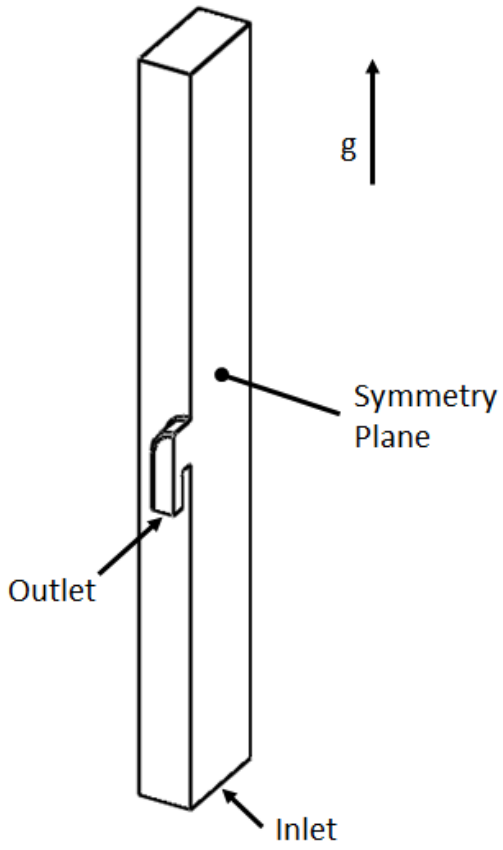

Figure 7-6 Diagram of the revised simulation domain

The revised simulation domain is dimensionally identical to that of the baseline simulation. Changes to the domain are indicated in Figure 7-6. There, the outlet, symmetry plane, and domain structure remain the same while the inlet has moved from the upper 'capping' surface to the lower 'capping' surface and the gravity vector has rotated 180° so as to reflect a rotation of the outlet-adjoining channel.

7.5.1 Parameters

Table 4 Revised domain simulation: material and boundary parameters

Parameter	Value	Units
Inlet Volumetric Flow Rate	0.1	[µL/min]
Plasma Density	1025	[kg/m3]
Red Blood Cell Density	1125	[kg/m3]
Hematocrit (HCT)	0.3	-
Plasma Viscosity	0.0015	[Pa*s]

7.5.2 Results

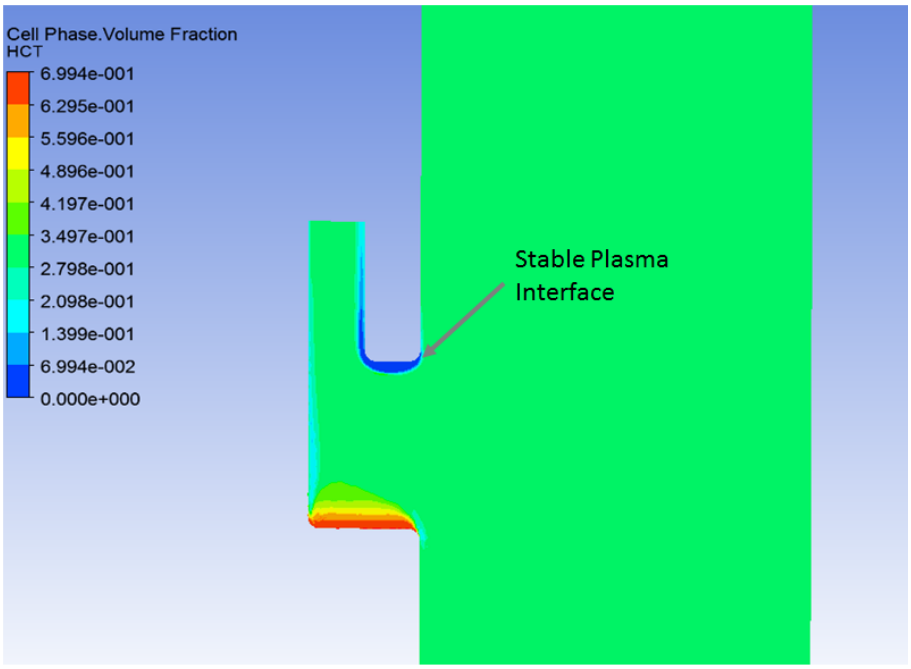

Figure 7-7 Plot of cell-volume fraction within the outlet region of the revised simulation domain

Figure 7-7 provides a plot of cell-volume fraction along the symmetry plane of the revised transport domain for time point (t=10[s]). Whereas in the baseline domain plasma

had gathered in the upper portion of the outlet-adjoining channel, the effective rotation of the domain has, as intended, reduced the extent of plasma-separation in the post-outlet region. Additionally, the packed-cell region at the bottom of the outlet-adjoining channel does not appear to result in a reversed flow into the blood-holding domain. Both of these findings are consistent with expectations and suggest that revision of the prior microdevice may be as simple as to rotate the outlet-adjoining channel 180°.

7.6 Experimental Testing of Revised Outlet-adjoining Channel

Numerical simulation of the cell-dispensing domain, having a revised outlet-adjoining channel, suggests that a simple reconfiguration of post-outlet geometry will eliminate the flow recirculation which had likely ailed the prior device (the device tested in Chapter 6). This design change was incorporated into a microdevice which utilized all of the key technical elements from the Chapter 6 microdevice; the two are functionally identical except for the outlet-adjoining channel.

7.6.1 Microdevice

The layout of the microdevice having a revised outlet-adjoining channel is shown in Figure 7-8. As noted in the previous section, the functional elements of the new device are nearly identical to the device tested in Chapter 6. The primary structural difference and only functional change between the two devices is a 180° rotation made to the outlet-adjoining channel.

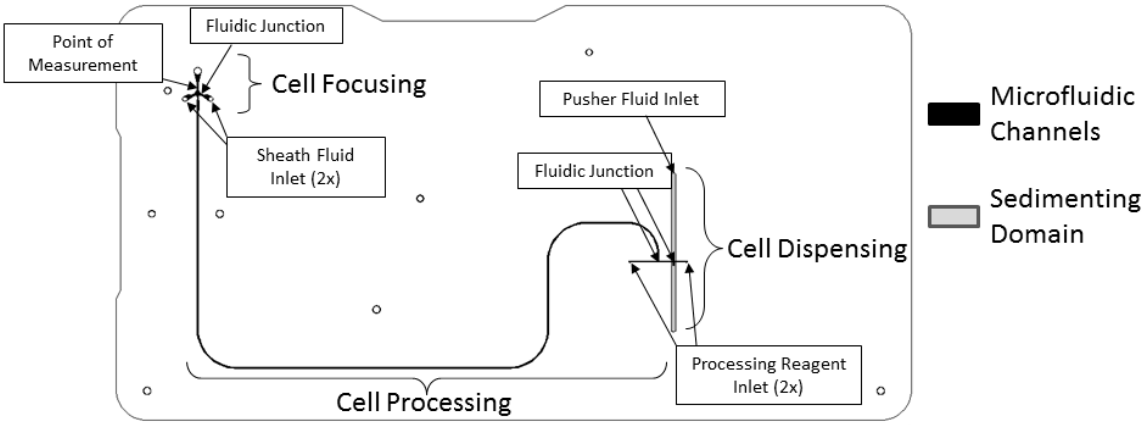

Figure 7-8 Annotated layout of the optimized microdevice with revised outlet-adjoining channel

7.6.1.1 Revised Outlet-Adjoining Channel

Figure 7-9 illustrates the transition of whole blood from the blood-holding volume to the cell-processing circuit within the new microdevice design. The revised outlet-adjoining channel is highlighted there. Whereas the flow within the outlet-adjoining channel in the Chapter 6 device had facilitated a downward flow, the revised channel conveys an upward flow. The direction of this flow is in keeping with the numerical simulation s from the prior section which had shown that an upward-moving outlet flow would relieve the build-up of plasma that had yielded an outlet-flow reversal in the prior microdevice.

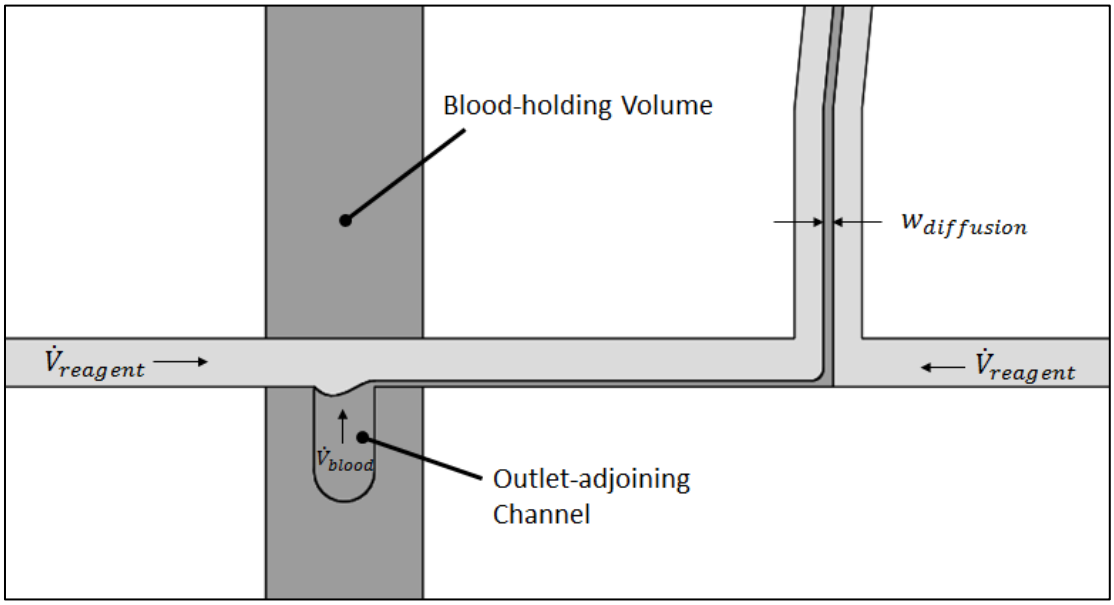

Figure 7-9 Detail view of whole blood transitioning from the blood-holding volume to the cell-processing circuit

7.6.2 Measurement Routine

The measurement routine used in this final set of testing was identical to the test routine utilized in Chapter 6:. The fluidic pumping rates and process timing for testing of the revised microdevice are detailed in routine 7A, provided in Appendix B.

7.6.3 Experimental Procedure

As with each of the prior two microdevices, experimental testing of the microdevice having both a gravity-negating dispense domain and revised outlet-adjoining channel consisted of RBC and WBC concentration measurement for a set of blood specimens having varied composition. In all, 12 unique samples were analyzed. For each sample

analysis, both an RBC and WBC concentration was generated. Each analysis was performed using the same measurement routine: routine 7A.

7.7 Results

7.7.1 RBC Concentration Measurements

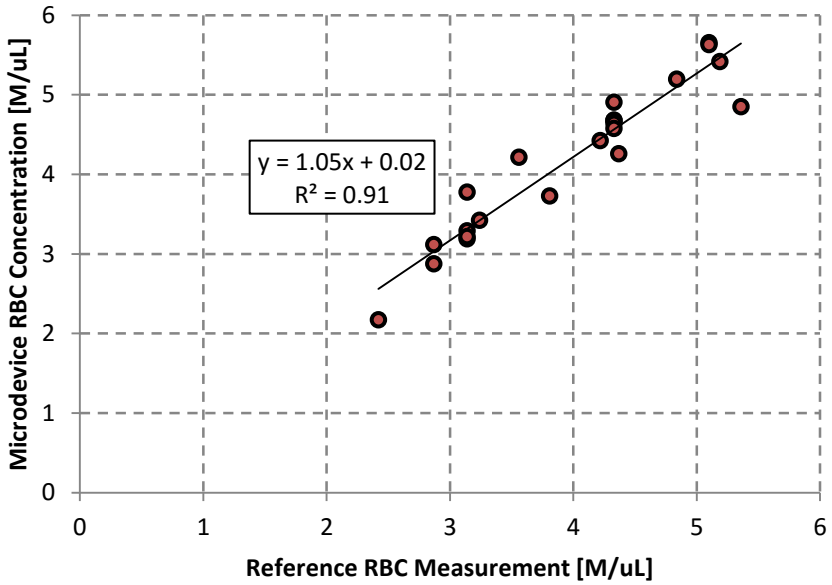

Figure 7-10 Scatterplot illustrating the correlation between microdevice and reference instrument measurements for RBC concentration

The RBC concentration of each sample was measured using both the optimized microdevice and reference instrument: an Abbott Cell Dyn 3200. A datum for each measurement is provided in Figure 7-10 which illustrates the correlation between RBC measurements made on the optimized microdevice and reference instruments. The data shows that the optimized device produced a stronger correlation ($R^2 = 0.91$ vs $R^2 = 0.85$)

and had better linearity relative to the reference instrument (slope = 1.05 vs slope = 0.65) than the initial microdevice.

7.7.2 WBC Concentration Measurements

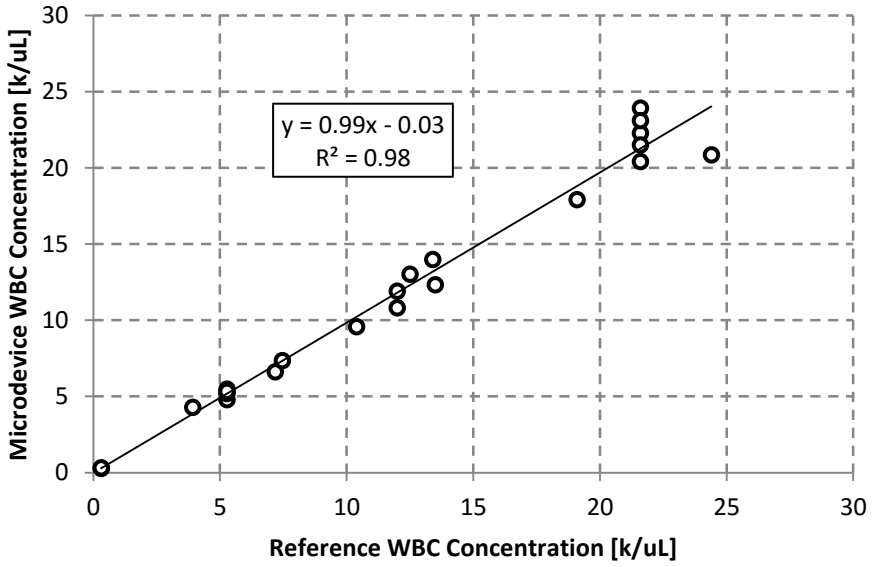

Figure 7-11 Scatterplot illustrating the correlation between microdevice and reference measurements of WBC concentration

The WBC concentration of each sample was measured using both the microdevice and reference instrument. A correlation of the measurements performed on each technology is provided in Figure 7-11. Again, the plot of WBC measurements show a stronger correlation (R^2 = 0.98 vs R^2 = 0.907) and closer unity to the reference instrument (slope = 0.99 vs slope = 0.62) than the initial microdevice.

7.8 Conclusions

The microdevice tested within this chapter differed minimally from the device tested in Chapter 6. In fact, the only functional change was to rotate the outlet-adjoining channel 180°. Numerical simulation of the revised cell-dispensing domain showed that the potential for an outlet-flow recirculation was minimized by this change. The experimental data confirms this notion. Whereas the previous version of the gravitationally-unbiased domain produced a general trend of inverse bias between RBC and WBC measurements, the revised device bias, shown in Figure 7-12, is distributed consistently about the x-axis as one would expect for a properly-functioning system.

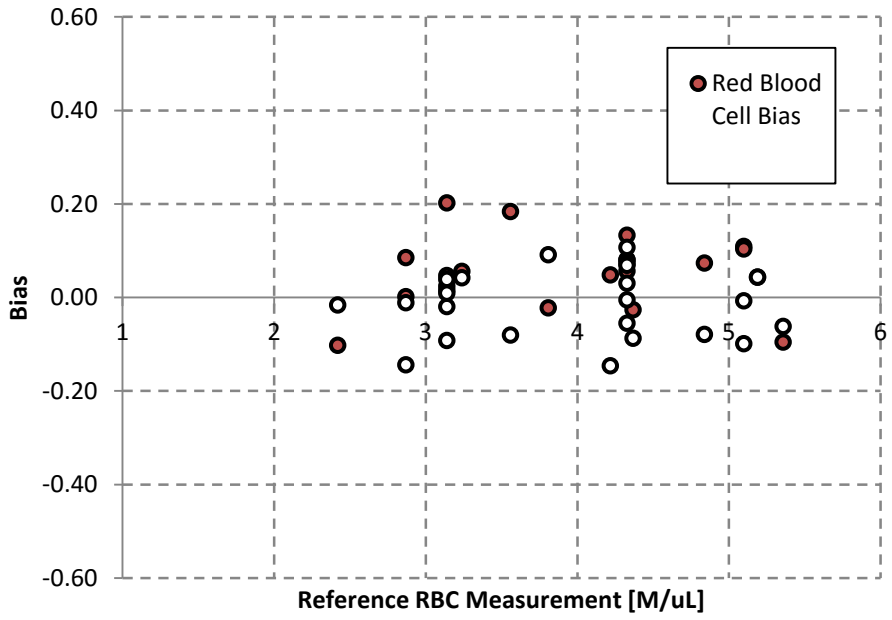

Figure 7-12 RBC and WBC biases for Concentration Measurements using the Optimized Microdevice

The relatively consistent bias across the biological range of RBC concentration shows stark contrast to the bias plot of measurements generated by both the initial device and the first iteration of the gravitationally-unbiased device. In each of the prior devices, RBC and WBC bias had bifurcated in the mid-to-low RBC range (see Figure 4-1) where the erythrocyte sedimentation rate becomes elevated. Independence of the cell-dispensing process from elevated ESR in the low-RBC-concentration range suggests that the optimized transport domain was extremely effective at negating the gravitational transport bias illustrated by the initial device as well as the reversed-outlet-flow bias within the prior device design.

Chapter 8: Summary of Results and Conclusions

This research was motivated by the desire to create a microfluidic technology which accurately quantifies the concentration of red and white blood cells within a whole blood specimen. Experiments performed utilizing an initial design suggested that whole blood transport would have a profound impact upon the efficacy of such a technology. Consequently, a great portion of this research emphasized characterization and analysis of cell transport within whole blood microflows.

Data interpretation and transport analysis drew heavily from the field of hemorheology, especially with regard to identification of the primary mechanics of cell transport within whole blood microflows. The established rheological mechanics were linked to in-device transport through a kinematic identity: derived in Appendix A. Post-hoc analysis of microdevice, cell-concentration measurements strongly suggested erythrocyte sedimentation as the primary mechanism affecting cell transport within the initial microdevice design. Additionally, a theory was generated in which cell margination (shear-induced inhomogeneity) was expected to affect cell transport in situations where the magnitude of bulk blood flow rate shifts in such a way that the normalized flow-domain velocity field changes due to the non-Newtonian properties of whole blood. From a practical standpoint, this conjecture raises concern for the potential impact of the manual introduction of blood specimens into a device wherein the rate of sample introduction is significantly more rapid than in-device operation. Specifically, a device

which does not maintain a homogeneous distribution of cells should yield a cell transport rate which is a complex function of the cross-sectional cell distribution and flow-rate-specific velocity profile. Because the normalized velocity profiles will differ between the 'device-loading' and 'operating' conditions, a homogeneous cell distribution is needed to ensure that the cell-transport rate scales proportionately to the bulk flow rate.

Ultimately, the learnings generated by analysis of the initial design informed a new, optimized, microdevice design which would support a cell-dispensing operation which was in close agreement to Equation (1-1). In the initial microdevice, an increase in channel cross section would exaggerate the effects of sedimentation. Because of this conflict, the cell transport domain had to be restructured in such a way that allowed simultaneous minimization of shear-induced cell inhomogeneity and minimization of sedimentation-based transport enhancement.

The optimized transport domain made use of the inherent 'stability' of the spatial distribution of cells in a sedimenting body of whole blood. By situating the outlet of the cell-dispensing transport domain at a location which, during the duration of a sample analysis, would be adjacent to the 'suspension' phase of the sedimenting whole blood, the effective concentration of dispensed cells would be constant. Moreover, said outlet was designed such that the outlet 'plane', separating the sedimenting domain from the device's microchannel segments, had a normal vector which was perpendicular to

gravity. As such, the gravity-parallel velocity imposed on cells by the sedimentation process does not affect the transport rate across the outlet. Conveniently, the gravity-negating action of the optimized cell-dispensing domain did not fundamentally rely on a minimization of the flow-domain cross section, thereby allowing the cross section of the sedimenting domain to be increased as necessary to avoid spatial inhomogeneity and shear enhancement of sedimentation.

On an initial pass, the re-designed transport domain had not produced significant gains in measurement accuracy. It was found, through numerical simulation, that the first version of the revised transport domain had likely been affected by and issue related to flow recirculation within the dispense circuit. Simulation also informed a revision to the circuit which promised to eliminate this recirculation. This revision was incorporated within a new, optimized cell-dispensing domain. The optimized cell-dispensing domain was tested in a microdevice in a manner comparable to the test procedure used to characterize transport in the initial device. The linearity (compared to a reference instrument) of device-generated RBC and WBC concentration measurements suggest that the optimized transport domain was an effective solution for negating the gravitational effects suffered by the initial device.

8.1 Characterization of Transport in Whole Blood Microflows

At the outset of this research, it was clear from the published literature that whole blood was an extremely well-characterized substance. However, there was a noticeable lack of publications relating the general ensemble of knowledge to cell transport in micro-scale, *in-vitro* blood flows. It seems likely that this paucity is due to the fragmented nature of the microfluidics field: technological challenges are largely application-specific. While whole-blood sedimentation has been a chief concern in devices covered here, its significance was brought about by the general approach adopted within the researched microdevices: displace a near-micro volume of whole blood, in an undiluted state, at a rate which is, practically speaking, as close to a no-flow condition as one can imagine. This is perhaps a rate-controlling aspect of the development of point-of-care diagnostics in general; each **new** application requires developers to overcome a truly unique set of technical challenges.

For the cell-counting application developed here, a chief concern was to control the rate of in-device cell transport through external control of the bulk volumetric flow rate of whole blood. While the technical solution produced by transport characterization was shown to be quite effective in controlling cell transport rates, the breadth of general fluids knowledge generated was limited by means of characterization and the depth of understanding provided by the primary reference field: hemorheology. Whole blood sedimentation, for instance, is a well-understood and easily-described process.

Subsequently, conclusions surrounding the effect of sedimentation upon RBC transport are concise and well-justified. Although the leukocyte anti-sedimentation process was derived from the RBC sedimentation process, descriptions of the WBC transport rate did not adhere as cleanly to experimental data generated by the initial device. There are many feasible explanations as to why WBC-transport defied logical description.

One of the biggest frustrations with regard to characterization of WBC transport was the lack of mathematical descriptions of leukocyte margination. Here, the likeliest secondary mode of transport bias (for WBCs) was not a mathematically-describable effect. In general, a lapse in theoretical tools can be supplemented with experimental characterization. While the studied microdevices provided quantitative feedback regarding cell transport rates, the cell kinematics which produced said transport rates would require direct observation of cell motion. To that end, a fluorescence imaging apparatus was attempted which would enable *in-situ* observation of WBC transport within whole blood. Due to the dense optical nature of red blood cells, white blood cells were found to be visible only near the surface of the flow domain; obscuring the pertinent region of flow.

With roadblocks on both the theoretical and experimental paths toward a technical solution, the transition from the initial microdevice to the optimized microdevice depended strongly on intuition. While a thorough developmental approach would

involve direct validation of the margination-negating effects of the optimized device, the WBC-transport rates indicated by concentration measurements have to supplement direct kinematic observation. Thus, while the optimized device appears to support well-controlled WBC transport, the 'device loading' effects described in Chapter 5 remain very much a hypothesis rather than a proven mechanism of transport.

From the perspective of an overview, this research was very successful in demonstrating the use of Equation (A-5) in analysis and description of in-device cell transport rates. This equation and its derivatives were developed specifically for this project as a means for relating cell kinematics, which are the focus of most established literature, to the cell-transport rates which were of chief concern here. This description enabled characterization of the initial device, formalization of the device-loading hypothesis, and explanation of the physical means by which the transition control volume produces controlled cell transport in the optimized device. Development and demonstration of this identity is, by a good measure, the most broadly-applicable product of this research.

8.2 Advancement of Point-of-Care, Cell-counting Technology

The realization of the initial microdevice to the optimized microdevice is the primary technological achievement of this research. As stated previously, the merits of the gravity-negating effects of the optimized device are predicated on the shortcomings of the initial device: a relatively artificial product of the cell-dispensing approach to cell enumeration. While the optimized transport domain is an application-specific

breakthrough, it is the application(s) which it promises to enable that is of interest. Because the value of point-of-care diagnostics is partly predicated on the expediency of results, it is important that a complete menu of diagnostic tests be available in a point-of-care format. To fill this menu is duty of application developers and is the path by which the optimized transport domain can contribute to the field of point-of-care diagnostics.

It would be too bold to state that any characterization provided within this report was an indication of the viability of the optimized microdevice for use in medical diagnostic settings. Aside from the extensive performance and reliability testing needed to make such a conclusion, development of a robust technology requires assurance of economical and usability traits which extend well beyond the scope of the present research. Thus, any technical solution which empowers a POC device should be judged solely on its ability to perform its intended function. The optimized transport domain is intended to facilitate the cell-dispensing procedure as a means to quantify red and white blood cell concentration in whole blood specimens. With regard to the latter, measurements generated by the optimized device suggest that the optimized transport domain is effective at facilitating in-device quantitation of cell concentration. Thus, the technological objective of this research, to advance cell-counting POC technology, was achieved.

References

[1] The Lewin Group, Inc., "The Value of Diagnostics Innovation, Adoption and Diffusion into Health Care," Falls Church, Virginia U.S.A., 2005.

[2] World Health Organization, "Increasing Access to Diagnostics Through Technology Transfer and Local Production," Geneva, Switzerland, 2011.

[3] D. Issadore and R. M. Westervelt, Point-of-Care Diagnostics on a Chip, Springer, 2013.

[4] World Health Organization, Decentralization in Health Care, McGraw-Hill, 2007.

[5] E. H. Slaats, "Hosptial Point-of-Care Testing - Quality Assurance and Clinical Acceptance," *Point of Care,* pp. 35-38, 2004.

[6] Centers for Medicare & Medicaid Services, "Medicare Part B Physician/Supplier National Data - CY 2007 Top 100 LAB PROCEDURES," 2007.

[7] S. K. Sia and L. J. Kricka, "Microfluidics and Point-of-Care Testing," *Lab on a Chip,* pp. 1982-1983, 2008.

[8] National Institutes of Health, *FACT SHEET - Point-of-Care Diagnostic Testing,* 2010.

[9] Renub Research, "Point of Care Testing Market and Forecast to 2016: Global Analysis," 2013.

[10] American Association of Diabetes Educators, "Practice Advisory - Blood Glucose

Meter Accuracy," 2013.

[11] C. P. Yeo, A. Ngo, W. Y. Ng and S. H. Lim, "Assessing Performance of the i-STAT at the Point of Care in the Emergency Room," *Proceedings of Singapore Healthcare,* pp. 157-161, 2011.

[12] C. D. Chin, V. Linder and S. K. Sia, "Commercialization of microlfuidic point-of-care diagnostic devices," The Royal Society of Chemistry, 2012.

[13] Sensirion AG, "LG16 Liquid Flow Meter Series; Compact Liquid Flow Meter for OEM Applications," September 2014 V2.

[14] H. M. Shapiro, Practical Flow Cytometry, John Wiley & Sons, 2005.

[15] Y. R. Kim and L. Ornstein, "Isovolumetric Sphering of Erythrocytes for More Accurate and Precise Cell Volume Measurement by Flow Cytometry," *Cytometry,* vol. 3, no. 6, pp. 419-427, 1983.

[16] R. Rannacher, A. M. Robertson and S. Turek, Hemodynamical Flows: Modeling, Analysis and Simulation, Basel, Switzerland: Birkhäuser Verlag AG, 2008.

[17] M. Brigden, "Clinical Utility of the Erythrocyte Sedimentation Rate," *Am Fam Physician,* vol. 60, no. 5, pp. 1443-1450, 1999.

[18] B. S. Bull, M. Caswell, E. Ernst, J. M. Jou, A. Kallner, J. A. Koepke, S. M. Lewis, G. D. O. Lowe, M. W. Rampling and K. Stuart, "ICSH recommendations for measurement of erythrocyte sedimentation rate," *Journal of Clinical Pathology,* vol. 46, no. 3, pp. 198-203, 1993.

[19] T. L. Fabry, "Mechanism of Erythrocyte Aggregation and Sedimentation," *Blood,* pp. 1572-1576, 1987.

[20] L. Bogar and M. Tekeres, "Leukocyte flotation during gravity sedimentation of the whole blood," *Clinical Hemorheology and Microcirculation,* vol. 22, no. 1, pp. 29-33, 2000.

[21] C. Lawrence and M. E. Fabry, "Erythrocyte Sedimentation Rate During Steady State and Painful Crisis in Sickle Cell Anemia," *The American Journal of Medicine,* pp. 801-808, 1986.

[22] U. Nobis, A. R. Pries, G. R. Cokelet and P. Gaehtgens, "Radial Distribution of White Cells during Blood Flow in Small Tubes," *Microvascular Research,* vol. 29, pp. 295-304, 1985.

[23] R. E. Wells and E. W. Merrill, "Influence of Flow Properties of Blood Upon Viscosity-Hematocrit Relationships," *Journal of Clinical Investigation,* vol. 41, no. 8, pp. 1591-1598, 1962.

[24] S. Chien, H. M. Usami, J. L. Taylor, J. L. Lundberg and M. I. Gregersen, "Effect of hematocrit and plasma proteins on human blood rheology at low shear rates," *Journal of Applied Physiology,* vol. 21, no. 1, pp. 81-87, 1966.

[25] G. R. Cokelet, E. W. Merrill, E. R. Gilliland, H. Shin, A. Britten and R. E. Wells, Jr., "The rheology of human blood- Measurement near and at zero shear rate.," *Trans. Soc. Rheol.,* vol. 7, pp. 303-317, 1963.

[26] R. Fåhraeus, *Acta med. Scand.*, vol. 55, no. 1, 1921.

[27] A. L. Copley, *Rheol. Acta,* vol. 1, p. 663, 1961.

[28] J. Goldstone, H. Schmid-Schonbein and R. Wells, "The Rheology of Red Blood Cell Aggregates," *Microvascular Research,* pp. 273-286, 1970.

[29] A. L. Copley, R. G. King and H. Ching-Row, "Erythrocyte Sedimentation of Human Blood at Varying Shear Rates," *Biorheology,* vol. 13, pp. 281-286, 1976.

[30] A. Jain and L. L. Munn, "Determinants of Leukocyte Margination in Rectangular Microchannels," *PLoS ONE,* vol. 4, no. 9, 2009.

[31] R. H. Phibbs, "Distribution of leukocytes in blood flowing through arteries," *American Journal of Physiology,* vol. 210, no. 5, pp. 919-925, 1966.

[32] R. Fahraeus, "The Suspension Stability of the Blood," *Physiological Reviews,* vol. 9, no. 2, pp. 241-274, 1929.

[33] S. Kallio and A. Akademi, "On the mixture model for multiphase flow," VTT Energy, 1996.

[34] J. J. Bishop, A. S. Popel, M. Intaglietta and P. C. Johnson, "Rheological effects of red blood cell aggregation in venous network: A review of recent studies," *Biorheology,* vol. 38, pp. 263-274, 2001.

Appendix A: Derivation of Kinematic Description of Cell Transport in a Straight Channel Segment of Uniform Cross Section

Describe the particle transport rate within a stream-wise element. Then, expand the description to apply to a closed channel particulate flow.

$$\dot{n}_{c.v.} = \frac{N_{observed\ at\ outlet}}{\Delta t_{observation}} \tag{A-1}$$

For an infinitesimal volume, the channel-wise velocity of bounded particles is uniform such that:

$$d\dot{n} = [c_{cell} * dA * ds] * \left[\frac{v_{\vec{s}} * dA}{ds * dA}\right] \tag{A-2}$$

Here, the first set of bracketed terms gives the quantity of cells bounded by the control volume and the second set of bracketed terms gives the ratio of channel-wise volumetric flow rate to the volume of the element. This equation can be simplified through cancellation of terms to give Equation (A-3).

$$d\dot{n} = c_{cell} * v_{\vec{s}} * dA \tag{A-3}$$

The surface integral of Equation (A-3), across the channel cross section, can be expressed by Equation (A-4) which states that the net transport within the channel is the sum of the individual elements spanning the channel cross section.

$$\dot{n}_{channel} = \sum c_i * \vec{v_s} * dA = \sum \frac{dN}{ds} \vec{v_s} \tag{A-4}$$

Equation (A-4) can be re-written in a manner which reflects a constant channel-wise length for the elements over which the summation is take which yields Equation (A-5). Equation (A-5) represents the channel transport rate as the summation of channel-wise cell velocities for all cells within the cross-section-spanning elements.

$$\dot{n}_{channel} = \frac{\sum \vec{v_{s,i}}}{ds} \tag{A-5}$$

The final step in deriving the desired description is to expand the observed region along the stream-wise direction so as to provide a volume-averaged transport rate, given in Equation (A-6).

$$\dot{n}_{channel} = \frac{\sum_{i=1}^{N} \vec{v_{s,i}}}{\Delta s} \tag{A-6}$$

Appendix B: Measurement Routine Tables

Routine 3A					
Step	1	2	RBC	4	WBC
Duration [s]	130	7	30	90	30
Pusher Fluid Flow Rate [µL/min]	1	1	Measurement	0.4	Measurement
Sphere Flow Rate [µL/min]	200	0		0	
Lyse Fluid Flow Rate [µL/min]	0	0		27	
Sheath Fluid Flow Rate [µL/min]	0	400		700	

Routine 3B					
Step	1	WBC	3	4	RBC
Duration [s]	135	30	90	7	30
Pusher Fluid Flow Rate [µL/min]	0.4	Measurement	1	1	Measurement
Sphere Flow Rate [µL/min]	0		200	0	
Lyse Fluid Flow Rate [µL/min]	27		0	0	
Sheath Fluid Flow Rate [µL/min]	700		0	400	

Routine 6A				
Step	1	RBC	3	WBC
Duration [s]	90	30	90	30
Pusher Fluid Flow Rate [µL/min]	0.2	Measurement	0.4	Measurement
Sphere Flow Rate [µL/min]	50		0	
Lyse Fluid Flow Rate [µL/min]	0		20	
Sheath Fluid Flow Rate [µL/min]	2000		1000	

Routine 7A				
Step	1	RBC	3	WBC
Duration [s]	90	30	90	30
Pusher Fluid Flow Rate [µL/min]	0.2	Measurement	0.4	Measurement
Sphere Flow Rate [µL/min]	50		0	
Lyse Fluid Flow Rate [µL/min]	0		20	
Sheath Fluid Flow Rate [µL/min]	2000		1000	